Iron mineral structure, reactivity, and isotopic composition in a South Pacific Gyre ferromanganese nodule over 4 Ma

Matthew A. Marcus [a,⇑], Katrina J. Edwards [b,1], Bleuenn Gueguen [c,d,e],

Sirine C. Fakra [a], Gregory Horn [b], Nicolas A. Jelinski [f], Olivier Rouxel [c], Jeffry Sorensen [f], Brandy M. Toner [f]

[a]Advanced Light Source, Lawrence Berkeley National Laboratory, Berkeley, CA 94720, USA

[b]Department of Biological Sciences, University of Southern California, Los Angeles, CA, USA [c]IFREMER,

Centre de Brest, Unité Géosciences Marines, 29280 Plouzané, France

[d]Institut Universitaire Europeén de la Mer, UMR 6538, Université de Brest, BP 80, F-29280 Plouzané, France [e]Department of Geology and Geophysics, Yale University, New Haven, CT 06520, USA

[f]Department of Soil, Water, and Climate, University of Minnesota, St. Paul, MN 55108, USA

Abstract

Deep-sea ferromanganese nodules accumulate trace elements from seawater and underlying sediment porewaters during the growth of concentric mineral layers over millions of years. These trace elements have the potential to record past ocean geochemical conditions. The goal of this study was to determine whether Fe mineral alteration occurs and how the speciation of trace elements responds to alteration over 3.7 Ma of marine ferromanganese nodule (MFN) formation, a timeline constrained by estimates from $^9Be/^{10}Be$ concentrations in the nodule material. We determined Fe-bearing phases and Fe isotope composition in a South Pacific Gyre (SPG) nodule. Specifically, the distribution patterns and speciation of trace element uptake by these Fe phases were investigated. The time interval covered by the growth of our sample of the nodule was derived from $^9Be/^{10}Be$ accelerator mass spectrometry (AMS). The composition and distribution of major and trace elements were mapped at various spatial scales, using micro-X-ray fluorescence (lXRF), electron microprobe analysis (EMPA), and inductively coupled plasma mass spectrometry (ICP-MS). Fe phases were characterized by micro-extended X-ray absorption fine structure (lEXAFS) spectroscopy and micro-X-ray diffraction (lXRD). Speciation of Ti and V, associated with Fe, was measured using micro-X-ray absorption near edge structure (lXANES) spectroscopy. Iron isotope composition ($d^{56/54}Fe$) in subsamples of 1–3 mm increments along the radius of the nodule was determined with multiple-collector ICP-MS (MC-ICP-MS). The SPG nodule formed through primarily hydrogeneous inputs at a rate of 4.0 ± 0.4 mm/Ma. The nodule exhibited a high diversity of Fe mineral phases: feroxyhite (d-FeOOH), goethite (a-FeOOH), lepidocrocite (c-FeOOH), and poorly ordered ferrihydrite-like phases. These findings provide evidence that Fe oxyhydroxides within the nodule undergo alteration to more stable phases over millions of years. Trace Ti and V were spatially correlated with Fe and found to be adsorbed to Fe-bearing minerals. Ti/Fe and V/Fe ratios, and Ti and V speciation, did not vary along the nodule radius. The $d^{56/54}Fe$ values, when averaged over sample increments representing 0.25–0.75 Ma, were homogeneous within uncertainty along the nodule radius, at 0.12 ± 0.07‰ (2sd, n = 10). Our results indicate that the Fe isotope composition of the nodule remained constant during nodule growth and that mineral alteration did not affect the primary Fe isotope composition of the nodule. Furthermore, the average $d^{56/54}Fe$ value of 0.12‰ we find is consistent with Fe sourced from continental eolian particles (dust). Despite

⇑ Corresponding author. Tel.: +1 510 495 2106; fax: +1 510 486 4102. E-mail address: mamarcus@lbl.gov (M.A. Marcus). [1]Deceased.

mineral alteration, the trace element partitioning of Ti and V, and Fe isotope composition, do not appear to change within the sensitivity of our measurements. These findings suggest that Fe oxyhydroxides within hydrogenetic ferromanganese nodules are out of

geochemical contact with seawater once they are covered by subsequent concentric mineral layers. Even though Fe-bearing minerals are altered, trace element ratios, speciation and Fe isotope composition are preserved within the nodule. Published by Elsevier Ltd.

1. INTRODUCTION

Marine ferromanganese nodules (MFN) have attracted interest for many decades due to their economic potential and their possible use as recorders of the marine geochemical environment over millions of years (Calvert and Cronan, 1978; Koschinsky and Hein, 2003). These nodules are among the slowest-growing natural materials known, with growth rates measured in mm/Ma, and characterized by alternating layers of Mn-rich and Fe-rich phases precipitated around a nucleus (e.g. shark tooth, rock debris) (de Lange et al., 1992; Banerjee et al., 1999). MFNs occur on the seafloor in water depths >4000 m, usually below the calcite compensation depth and in well oxygenated environments. They generally form in inactive tectonic settings where very slow rates of sedimentation (<10 cm/1000 years) protect metals from dilution with background sediments. The abyssal plains, such as the Clarion-Clipperton zone in the Central Pacific Ocean have the most abundant nodule fields at the seafloor (Hein et al., 2013). MFNs are different from ferromanganese crusts that are deposited in shallower environments mostly on the flanks of seamounts by hydrogenous precipitation from dissolved trace metals in seawater. The sources of metals to MFNs can include: (1) a hydrogenetic source, (2) a diagenetic source, largely derived from the decay of organic matter, and (3) a hydrothermal source. The diagenetic source is generally considered predominant, indicating the important role of organic matter decay during early diagenesis processes in oxic sediments that release dissolved trace metals to sediment porewaters (Klinkhammer et al., 1982; Sawlan and Murray, 1983; Heggie et al., 1986; Morford and Emerson, 1999). However, hydrogenetic nodules do form under low-productivity waters. In addition, microorganisms have been proposed as geochemical agents in Mn- and Fe-cycling in sediments leading to the formation of MFN (Wang et al., 2009), whereas sorption experiments of Ni on ferrihydrite showed that the presence of organic material decreased the sorption efficiency of Ni on the mineral (Eickhoff et al., 2014).

Iron is often the most or second-most abundant metal in MFNs, and is present as Fe-bearing mineral phases known to be chemically reactive with trace elements. For instance, rare earth elements in MFN are thought to be hosted by the Fe-phases (Elderfield et al., 1981). Although the properties of Mn minerals and trace elements in MFNs have been examined many times over the past decades (Cronan, 1975; Elderfield et al., 1981; Dymond et al., 1984; Aplin and Cronan, 1985; Banakar and Tarkian, 1991; MartinBarajas et al., 1991; Yoshikawa, 1991; Verlaan et al., 2004), there has been comparatively little research on Fe mineral phases. This is likely due to analytical difficulties associated with distinguishing among the suite of Fe oxyhydroxide phases that may occur, as well as the fine spatial scale over which mineralogy varies in nodules. The use of traditional techniques such as powder X-ray diffraction (XRD) and ^{57}Fe Mossbauer spectroscopy has been largely unsuccessful due to the poorly crystalline, distorted structures, and intergrowth with Mn oxides (Murad and Schwertmann, 1988). Further, most of the literature on MFN mineralogy is unreliable; for example, it was once typical to identify a Mn-rich phase as ''todokorite'' based on optical microscopy and perhaps a bulk XRD pattern. Synchrotron X-ray microprobe (lXRF, lXAS and lXRD) techniques allow us to tackle these issues on unprocessed samples (Manceau et al., 2002). To date, this approach has been used infrequently, but successfully, to study the incorporation of trace elements in nodule nanophase oxides and using marine ferromanganese deposits as natural long-term sorption laboratories (Takahashi et al., 2000, 2007; Marcus et al., 2004b; Manceau et al., 2014).

Despite the analytical challenges, the structure and reactivity of Fe minerals in MFNs must be defined if we wish to validate them as recorders of past marine conditions. Specifically, mineral transformation processes may result in a blurring or over-writing of trace element speciation and isotopic signatures. For example, it is known that trace metal associations (e.g. Ni, Zn) with Fe minerals (e.g. goethite) can change in the presence of Fe^{2+} under laboratory conditions, especially under advective flow conditions (Frierdich et al., 2011; Frierdich and Catalano, 2012). Ferrihydrite in particular has been shown to incorporate additional Cu and Zn during Fe^{2+} catalyzed recrystallization, as reviewed by Latta et al. (2012). From a Mn mineral perspective, it has been demonstrated in laboratory studies that Ni uptake by the Mn oxide birnessite is pH dependent, but also reversible, calling into question its use as a paleopH indicator (Peacock, 2009). However, transition metals such as Ni, Mn, and Co have been shown to slow the rate of recrystallization of poorly ordered Fe oxyhydroxides (Cornell et al., 1992); which could result in preservation of the original chemical association between the mineral and trace element. Perhaps the primary factor in preservation of trace element signatures is the degree to which buried mineral layers are in geochemical contact with younger deposits and current seawater conditions. If recrystallization creates Fe mineral phases with similar reactive properties and the mineral is out of contact with seawater, then we might expect the preservation of trace element signatures over time in nodules.

In the present contribution, we use a variety of spectroscopic and isotopic approaches to address whether Fe minerals transform to stable phases in a South Pacific Gyre over time. In addition, we ask whether Fe minerals can retain the geochemical signatures of associated trace elements and faithfully record the Fe isotope composition of seawater through time.

2. NODULE DESCRIPTION AND METHODS

2.1. Description of the sample

2.1.1. Sample collection and handling

The nodule was collected December 24, 2006 (D'Hondt et al., 2009), at 2603.09⁰S, 15653.65⁰W, at 5126 m water depth during the Knox02RR cruise of the RV Roger
Revelle, using a multicore sampler. The site, South Pacific Gyre-2 (SPG-2), is characterized as follows: SPG-2 is located in a region of abyssal hill topography trending roughly NE-SW (065). Two populations of abyssal hill topography are present. The larger hills have relief ranging from 300 to 400 m with a spacing of 20 km. The smaller hills are superimposed on the larger abyssal hills and have a relief of about 50–100 m and a spacing of about 5–6 km. Several small seamounts (2 km-wide, 300 m-high) are scattered about the region. The largest seamount is located 3–4 km south of the coring site.

The coring site is located within magnetic polarity Chron 34n so the crustal age may range from 84 to 124.6 Ma (Gradstein and Ogg, 2002). Based on a tectonic reconstruction of the region (Larson et al., 2002), the crust was accreted along the Pacific-Phoenix spreading center 95 Ma ago at ultra-fast spreading rates (90 km/Ma, half-rate). The sediment on which the nodule rested (halfburied) was homogeneous dark brown clay with micronodules and no microfossils seen on a smear slide. The nodule described in this study was approximately spherical (diameter was 65–68 mm as obtained from nine measurements along three axes) and was observed shipboard to be partially buried in sediment at the top of the sediment core. However, the actual orientation of the nodule at the seafloor is not known. The sample was collected as part of a much larger effort to document the nature of life in slowly-accumulating sediments of low primary productivity and great age.

A polished petrographic thin section of the nodule was prepared by Spectrum Petrographics, Inc. The nodule was embedded in 3 M Scotchcast #3, mounted on a fused silica slide with Loctite Impruv 363 adhesive, and sectioned to a 30 lm slice and diamond-polished to an electronmicroprobe finish. In addition, 1 mm-thick sections were made and cut into 2 mm-wide ''matchsticks'' for X-ray tomography, wet-chemical analysis and lXRD.

2.1.2. Chemical composition

The ''matchstick'' nodule sample was sectioned lengthwise into 10 sub-samples using a microdrill device (Micromill). Each fraction was dissolved in a mixture of 6 mL concentrated HNO_3 (sub-boiled) and 2 mL concentrated HF (Trace metal or Optima grade) to ensure complete dissolution of silicate phases. Solutions were evaporated on hot plates at 80 C. Dry residues were then dissolved in 5 mL concentrated HNO_3 and 5 mL 6 M HCl and evaporated to dryness at 80 C. This last step was repeated once to ensure completed dissolution of non-siliceous materials including fluorides that could have formed during the first digestion step. Archive solutions were kept in 5 mL 6 M HCl. Elemental concentrations were measured on an ICP-AES (Inductively Coupled Plasma Atomic Emission Spectroscopy instrument, HORIBA Jobin YVON,
ULTIMA 2) operated by Poˆle-Spectromeˊtrie-Oceˊan (PSO, Ifremer/IUEM, Brest, France). Calibration of the

concentrations during analysis was done using a multi-elemental solution. As a consistency check, two geostandards of nodule samples (USGS Nod P1 and USGS Nod A1) were analyzed alongside our samples. The results, shown at the bottom of Table 1, are consistent with published data (Axelsson et al., 2002).

Due to the process involved in micro-drilling and ICPAES analysis, and potential dilution by embedding resin, the nodule material could not be accurately weighed, but about 10 mg was collected for each subsample. Therefore, for consistency and comparison with electron microprobe geochemical data, we did not report ICP-AES data in microgram of element per gram of rock as it is the common usage in geochemistry, but instead data were normalized to Fe and expressed in grams of element per gram of Fe. We defined two different zones in the nodule, the ''inner'' and the ''outer'' nodule zones. The ''outer'' zone corresponds to the most external layers including the surface directly in contact with ambient seawater. Therefore, the ''inner'' zone is also the oldest and the ''outer'' zone is the youngest zone of the nodule. These zones are morphologically distinct, as shown in Figs. 1 and 3 and discussed below. Note that our section of the nodule does not include the part in contact with the nucleus.

The fine-scale elemental composition and mineral textures was examined with electron microprobe analysis using a JEOL JXA-8900 Electron Probe Microanalyzer and wavelength-dispersive spectrometer at the Electron Microprobe Laboratory, Earth Science Department, University of Minnesota.

2.2. Nodule material relative age estimates and apparent growth rate

2.2.1. ⁹Be/¹⁰Be systematics

Most relative age estimates and apparent growth rates of Fe–Mn nodules have been constrained by relying on the unique characteristics of the $^9Be/^{10}Be$ system in oceanic environments (Graham et al., 2004). The delivery of ^9Be (the stable Be isotope) and ^{10}Be (a long-lived radioisotope of Be with a half-life of 1.39 Mya) to well-mixed deep ocean waters and their subsequent incorporation into growing Fe–Mn nodules can be used as a proxy for the relative ages of nodule sections when differences in the concentration of ^{10}Be or $^9Be/^{10}Be$ ratio with depth in the nodule are known (Segl et al., 1989; Graham et al., 2004). Although many processes contribute to the ultimate concentrations and ratios of ^9Be and ^{10}Be in ocean waters, two important general principles apply: (1) the delivery of ⁹Be to oceans is primarily from terrestrial sediments and

Nodule section #	Distance from nodule surface (mm)**	Al/Fe	Ba/Fe	Ca/Fe	Ce/Fe	Co/Fe	Cu/Fe	K/Fe	La/Fe	Mg/Fe	Mn/Fe	Mo/Fe	Na/Fe	Ni/Fe	P/Fe	Sr/Fe	Ti/Fe	Zn/Fe	Cu/Ni	$d_{56/54}Fe_{IRMM-14}$	2sd***	$d_{57/54}Fe_{IRMM-14}$	2sd***
N1 (Outer)	3	0.184	0.0085	0.119	0.0114	0.035	0.0096	0.047	0.0015	0.0843	1.14	0.0019	0.123	0.0217	0.017	0.0064	0.106	0.0036	0.45 0.165 0.0081	0.16	0.09	0.19	0.10
N2	6	0.109	0.0093	0.030	0.0076	0.040	0.0014	0.0634	0.93	0.0016	0.095	0.0138	0.016	0.0057	0.105	0.0030	0.55	0.214 0.0078	0.122 0.0096	0.09	0.09	0.01 0.19	0.10
N3	8	0.034	0.0089	0.054	0.0015	0.0763	1.04	0.0018	0.107	0.0184	0.019	0.0060	0.104	0.0035	0.48	0.191	0.0080	0.150	0.0095 0.031 0.0095		0.09		0.10
N4	10	0.040	0.0015	0.0714	1.10	0.0018	0.106	0.0215	0.022	0.0060	0.095	0.0038	0.44	0.199	0.0083	0.150	0.0104	0.034 0.0094	0.032 0.0014	0.17	0.09	0.17	0.10
N5	12.5	0.0747	1.25	0.0022	0.115	0.0241	0.016	0.0066	0.087	0.0039	0.39	0.215	0.0077	0.141	0.0096	0.028	0.0084	0.032 0.0013	0.0677 1.04	0.14	0.09	0.14	0.10
N6	13.5	0.0019	0.099	0.0182	0.016	0.0060	0.079	0.0037	0.46	0.227	0.0072	0.126	0.0089	0.027	0.0084	0.037	0.0011	0.0672 1.02	0.0020 0.103		0.09	0.06	0.10
N7	14.5	0.0169	0.015	0.0056	0.071	0.0038	0.50	0.193	0.0076	0.112	0.0100	0.031	0.0085	0.038	0.0012	0.0688	1.02	0.0021 0.098	0.0179 0.015	0.07	0.09	0.21	0.10
N8	16	0.0058	0.076	0.0040	0.48	0.188	0.0071	0.110	0.0111	0.034	0.0082	0.033	0.0012	0.0724	1.02	0.0022	0.092	0.0183	0.016 0.0056 0.083	0.10	0.09	0.17	0.10
N9	18	0.0040	0.45																	0.16	0.09	0.16	0.10
N10 (Inner)	19.5	0.160	0.0073	0.099	0.0133	0.026	0.0083	0.022	0.0012	0.0682	0.92	0.0022	0.084	0.0178	0.017	0.0055	0.075	0.0043	0.46	0.09	0.08	0.18	0.11
USGS Nod-P-1	–	0.379	0.0448	0.395	0.0064	0.041	0.2113	0.193	0.0021	0.3360	5.10	0.0106	0.304	0.2504	0.027	0.0114	0.052	0.0306	0.84 0.197 0.01400.49 0.40		0.07	0.69 0.55	0.11
USGS Nod-A-1	–	1.129	0.0079	0.031	0.0103	0.048	0.0013	0.2647	1.73	0.0035	0.081	0.0634	0.041	0.0145	0.033	0.0059	0.16				0.09		0.10

Table 1

Inner (a) Full radius transect Outer

1 mm

(b) Outer
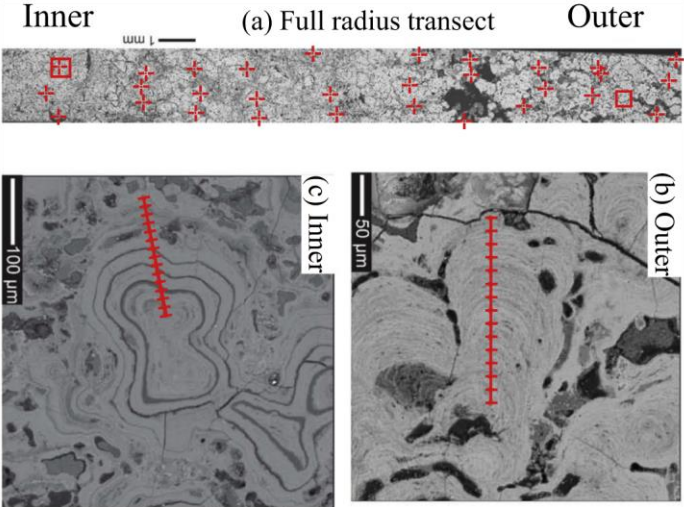
50 µm

(c) Inner

100 µm

Fig. 1. Backscatter SEM images showing "outer" and "inner" regions. Red lines and crosses show locations of electron microprobe analyses displayed in Fig. 4. The red line in (b) transects an individual botryoidal structure. (For interpretation of the references to color in this figure legend, the reader is referred to the web version of this article.)

is thus (at least outside of sediment plumes at continental shelves) influenced by globally averaged erosion rates, and the position of the delivery of

Be to ocean is primarily due to direct deposition of cosmogenic production in the upper atmosphere (due to spallation reactions involving high-energy cosmic particles and gaseous O and N atoms) and is therefore dependent on the long-term variation of isolar activity (Willenbring and von Blanckenburg, 2010b). Both of these factors are known to vary over time, however erratios appear to vary around a long-term mean (Willenbring and von Blanckenburg, 2010a) and growth rate estimates from

[10]Be remain the major tool available to constrain and assess differences in ferromanganese nodule growth behavior due to environmental factors.

2.2.2 Chemical extraction and determination of [9]Be and [10]Be concentrations were determined in two increments between 0–5 mm and 15–20 mm (as measured from the nodule core) from the nodule cross-section ("inner" and "outer", respectively). Material from the section was extracted in three parallel sections. The middle material was used for [10]Be determination and the two outer sections used for [9]Be determination.

Be was determined by extracting approximately 0.25 g of ground nodule material in 6 M HCl for 3 h at 110 C. Samples were analyzed in a Thermo Scientific X SERIES ICP-MS with ESI PC3 Peltier cooled spray chamber,

(2)

Bulk chemical analyses of the nodule section measured by ICP-AES[*] and $d^{56/54}Fe$ values (‰) measured by MC-ICP-MS.

[*]
Concentrations are given in grams of element per gram of Fe (i.e. Element/Fe ratios).

[**]
Distance from outer nodule is reported as the distance from the top surface of the nodule.

[***]
2sd was determined on replicate measurements of the Fe isotopic standard IRMM-14. See text for explanations.

SC-FAST injection loop, and SC-4 autosampler (Aqueous Geochemistry Laboratory, Earth Science Department, University of Minnesota). Samples were diluted 20 and 20 ppb of Y internal standard was added. [10]Be was extracted from the nodule material through a series of acidification steps and cation column chromatography prior to being oxidized and analyzed by AMS. The methodology used here is modified from Ebert et al. (2012). Approximately 0.25 g of ground nodule material was extracted in Teflon vessels with 6 M HCl and 250 lg of spiked [9]Be carrier at 110 C for 3 h. 4 ml of HF was added to the cation solution in two steps to bind excess Ca and Mg. After each HF addition step, 2 mL of ultrapure H_2O_2 was added to remove organics. The ultrapure water containing Be and other cations was removed from the fluoride cake via centrifugation and pipetting. Ion exchange chromatography (both anion and cation removal steps) was used to purify Be cations from the bulk cation solution. Be-hydroxides were precipitated from the purified cation solution by titration to pH 9 through the addition of ammonium hydroxide. The supernatant was decanted and the precipitate was washed several times with ultrapure water and dried overnight at 100 C in low-boron quartz vials. The dry precipitate was flame-oxidized at >850 C to form BeO powder and pressed into cathodes for AMS analysis at PRIME Lab, Purdue University, USA.

2.2.3. Growth rate estimation

The nodule growth rate was estimated by the [10]Be dating method developed for ferromanganese nodule segments (Baturin and Savenko, 1989; Somayajulu, 2000; Graham et al., 2004). This dating method is based on the relative difference in isotopic composition of two layers (Graham et al., 2004):

Age difference ¼ ð$t_{1=2}$=ln2ÞÞln ðI=OÞ

where $t_{1/2}$ is the half-life of [10]Be, and I and O are the isotopic composition of the ''inner'' and ''outer'' increments, respectively. The average growth rate between segments can then be determined by dividing the age difference by the distance across the nodule cross-section measured between segment centroids. Several previous growth rates reported for ferromanganese nodules used the older halflife estimate for [10]Be of 1.5 ± 0.1 Ma (Bhat et al., 1973). Here, we report absolute growth rate estimates using the revised consensus half-life for [10]Be (Chmeleff et al., 2010; Korschinek et al., 2010) of 1.387 Ma and also report apparent growth rate estimates using the former value of 1.5 Ma to facilitate direct comparison with previous work (i.e. Graham et al., 2004). The major assumptions of this equation is that the layers concerned had the same initial isotopic concentration when they were formed, and that there has been no isotopic exchange or fractionation since that time.

Some authors have applied the isotopic ratio of [10]Be/[9]Be of the segments, instead of bulk [10]Be concentrations (atoms g[1]) to calculate age differences as there is evidence that the [10]Be/[9]Be ratio of seawater is more invariant over time than the absolute [10]Be concentration (Segl et al., 1989; Graham et al., 2004). Therefore, we report age differences and growth rates here based on both the Be isotopic ratio and absolute [10]Be concentrations.

2.3. lXRF, lXAS, and lXRD

In order to study the morphology and elemental distributions in more detail micro X-ray fluorescence (lXRF) maps were acquired at Beamline 10.3.2 of the Advanced Light Source (Marcus et al., 2004a). For a general survey, a long map was acquired over a strip 20 mm long by 1 mm wide, with 20 lm pixels. All lXRF maps on the nodule were acquired at 10 keV, using dwell times of 30–50 ms and pixel sizes of 5–10 lm. Fluorescence emission signals for Fe, Mn, Ni, Cu, Zn, Ti, Ca, and additionally in some areas Ce, V, P and Co were recorded with a sevenelement Ge solid state fluorescence detector (Canberra).

Micro-X-ray absorption spectra (lXAS) at the Fe, V and Ti K-edges were recorded in fluorescence mode on selected spots of the lXRF maps. The energy was calibrated with respect to the respective metal foils, whose inflection-point energy were taken to be 7110.75 (Fe), 5463.76 (V) and 4966.40 eV (Ti) respectively. Data were calibrated, deadtime-corrected, pre-edge subtracted and post-edge normalized using custom LabVIEW programs available at the beamline (https://sites.google.com/a/ lbl.gov/microxas-lbl-gov/software). The data range for micro X-ray absorption near edge structure (lXANES) spectroscopy was 100 eV below up to 300 eV above the edge, while micro extended X-ray absorption fine structure (lEXAFS) spectroscopy data were taken up to 500 eV above the edge. Fe lXANES spectra were fit by leastsquare linear combination (LCF) to a large Fe database (Marcus et al., 2008). Over-absorption is significant in the more Fe-rich spots, and is taken as a free parameter in a simple model (planar, thick sample). Since the cited paper was published, a number of new spectra were added, including one for feroxyhite, a potentially-important species for nodules. This sample was prepared by the method of Schwertmann and Cornell (2000) and verified by powder XRD at the Characterization Facility, University of Minnesota, using a Siemens D-500 diffractometer with cobalt source. The observed [Si]/[Fe] ratios in the nodule are low enough to rule out the presence of a significant (>10%) amount of clays or most other silicates, so these were omitted from the set of fitting references. For V and Ti, our libraries are much more limited. For Ti, the only standard we had whose XANES was at all similar to that of the sample was ilmenite. For V, we used samples of V(V) sorbed on d-MnO_2 and ferrihydrite. Hexagonal birnessite ($K_{0.5}Mn_2O_4$ 1.5H_2O) was synthesized by published methods (McKenzie, 1971; Villalobos et al., 2003) using purified water (18.2 MO; MilliQ) and ACS grade reagents. Briefly, hexagonal birnessite was prepared by boiling a 2.5 L solution of 0.4 mol/L $KMnO_4$ with vigorous mechanical stirring. The precipitate was formed through drop wise addition of 163 mL of concentrated HCl using a burette. V adsorption experiments were performed using goethite and 2-line ferrihydrite, synthesized by standard procedures (Schwertman and Cornell, 1991).

The precipitates were washed in 3 centrifuge-resuspend cycles with purified water, separated from suspension using vacuum filtration (0.22 lm Millipore polyethersulfone), and then

freeze dried and stored as a dry power. Fe micro-EXAFS spectra were analyzed with $k^3v\partial k\text{Þ}$ weighting, out to k = 11 A$^{\circ}$ ^{1}. For those spectra in which over-absorption was significant, we performed LCF of the XANES spectra to estimate the amount of overabsorption, applied that correction to the post-edge normalized spectra, and extracted the EXAFS signal from these corrected spectra. EXAFS data were then fitted using either linear combinations of reference EXAFS spectra or by shell-by-shell fitting using Artemis (Newville, 2001; Ravel and Newville, 2005). For the latter, the structures of goethite and lepidocrocite were used to create FEFF6l input files from which to extract Fe–O and Fe–Fe paths out to 3.5 A$^{\circ}$, which encompasses face, edge, and cornersharing FeO_6 octahedra. This analysis is similar to the polyhedron-centered analysis which was done for poorlyordered biogenic Fe oxide (Toner et al., 2009). For some of the spectra, we used a shell-by-shell fitting approach based on experimental amplitudes and phases (feroxyhite and lepidocrocite, for Fe–O and Fe–Fe paths), which gave results consistent with the Artemis fitting.

Micro XRD patterns were recorded with a Bruker SMART6000 CCD at 17 keV (k = 0.7293 A$^{\circ}$) and 240 s acquisition time. The patterns were radially-integrated and calibrated using alumina powder and fit2D software (Hammersley, 1997). Micro XRD patterns were recorded at the lXAS spot locations on the thin sections, and on a nearby blank spot on the silica substrate so as to background subtract the data. In order to improve the sensitivity of the XRD, we also mounted a thick section (''matchstick'') in such a way that the beam passed through 1 mm of sample without striking the substrate.

2.4. Fe isotope analyses

Iron isotope compositions were analyzed on a multi collector (MC-) ICP-MS (Inductively-Coupled-Plasma Mass-Spectrometer) (Neptune, Thermo-Scientific) at PôleSpectromé̀trie-Océan (PSO, Ifremer/IUEM, Brest, France) on the 10 subsamples of the nodule analyzed for the bulk geochemistry (see Section 2.1.2). After chemical separation of Fe from the matrix through chromatography columns filled with an anion-exchange resin AG1-X8, $^{56}Fe/^{54}Fe$ and $^{57}Fe/^{54}Fe$ isotope ratios were measured using a nickel-doping method to correct samples for instrumental mass discrimination combined with a standard-samplebracketing method (Albaràde and Beard, 2004; Rouxel et al., 2005, 2008) This analysis scheme allows us to determine a 2r of 0.07–0.09‰ based on replicate measurements of IRMM-14 isotopic standard. $^{56}Fe/^{54}Fe$ isotope ratios of samples are reported relative to IRMM-14 Reference Material according to the conventional delta notation (1) used for stable isotope systematics: $d_{56=54}Fe$ ¼ ½$\partial_{56}Fe_{=54}Fe_{sample}$Þ=$\partial_{56}Fe_{=54}Fe_{IRMM-14}$Þ 1 1000 ∂^1Þ The relationships between $d^{56/54}Fe$ and $d^{57/54}Fe$ of the samples analyzed in this work plot on a single mass

fractionation line and only $d^{56/54}Fe$ values are discussed in this paper.

The iron isotope composition of the USGS geological reference material nodule (Nod-A-1), yielding $d^{56/54}Fe = 0.37 \pm 0.06$ (2sd, n = 12) is consistent with previously published data (Dideriksen et al., 2006). We also determined the long-term average value of Nod-P-1 USGS geological reference material and obtained $d^{56/54}Fe = 0.51 \pm 0.09$ (2sd, n = 11). Results for Nod-A-1 and Nod-P-1 reported in Table 1 correspond the $d^{56/54}Fe$ values obtained within the same analytical conditions than for the nodule samples obtained after micro-drilling.

3. RESULTS

3.1. Nodule growth rate

The chronometer we used was based on two Be isotopes, ^{9}Be and ^{10}Be. ^{10}Be is a radioactive nuclide produced in the atmosphere (cosmogenic nuclide). The production rate of ^{10}Be in the atmosphere is dependent largely on solar activity and when this flux reaches the oceans through wet and dry deposition, it mixes with ^{9}Be present in the oceans after riverine inputs. The seawater isotope ratio of $^{10}Be/^9Be$ has varied around a long-term mean in modern oceans (Willenbring and von Blanckenburg, 2010a,b), and when nodules precipitate from seawater they incorporate Be which has the same $^{10}Be/^9Be$ ratio as ambient seawater. ^{10}Be decays with a half life of 1.39 Ma (Chmeleff et al., 2010) and therefore as the nodule grows, both absolute ^{10}Be concentrations and $^{10}Be/^9Be$ ratios in the older layers of the nodule will decrease. Using the exponential law of radioactive decay we can reconstruct an age model for the different layers in the nodule (Sections 2.2.1 and 2.2.3).

The ^{9}Be and ^{10}Be values for the nodule are displayed in Table EA1. Both ^{9}Be and ^{10}Be concentrations for this nodule (3.6–3.8 mg/kg and 0.54–3.41 10^9 atoms g^1, respectively) fall within the range of concentrations reported in previous publications (Segl et al., 1989; Graham et al., 2004). The growth rates estimated for this nodule (from 3.8 ± 0.7 to 4.2 ± 0.7 mm/Ma) using multiple estimation methods appear to be slightly lower than the range of rates reported in Graham et al. (2004) (4.7– 32 mm/Ma), but are well within the range of other globally compiled estimates (1.24–5.17 mm/Ma) from Willenbring and von Blanckenburg (2010a).

3.2. Chemical composition

The chemical composition of the South Pacific Gyre-2 (SPG-2) nodule, as determined by analyses of 10 increments spanning the 19.5 mm radius of the nodule in 1–3 mm lengths, is displayed in Table 1. All elemental concentrations are normalized by Fe. In addition to the bulk average of the 1–3 mm increments, Electron Microprobe Analysis (EMPA) was used to measure fine-scale elemental composition in three transects displayed in Fig. 1. The EMPA data are expressed in wt%, but note that the sum of the weights does not equal 100% because the nodule is

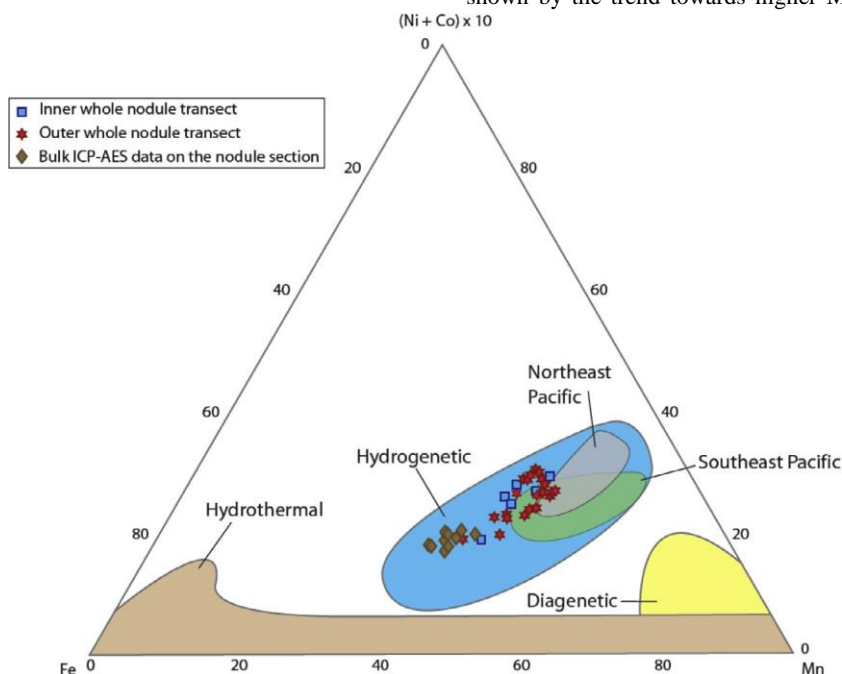porous, rich in hydrous mineral phases, and CO_2 (Tables EA2 and EA3).

Fig. 2. Ternary diagram of Fe, Mn and (Ni + Co) 10 (adapted from Bonatti et al., 1972) of Electron Microprobe data acquired along a transect through the whole nodule and bulk ICP-AES measurements on the nodule section. The distinction between ''inner'' and ''outer'' regions is explained in Table EA2 and in the text. This diagram allows to distinguish between three different fields (hydrothermal, hydrogenetic and diagenetic) indicating the predominant origin of the Fe/Mn-rich deposits formation. Selected literature data from Southeast Pacific nodules (green field) (Halbach et al., 1981) and Northeast Pacific (gray field) (Halbach et al., 1981) are included for comparison. (For interpretation of the references to color in this figure legend, the reader is referred to the web version of this article.)

Fig. 2 shows a ternary plot of Mn, Fe and (Ni + Co) 10 and displays the properties distinguishing among hydrothermal, hydrogenetic, and diagenetic sourced marine Fe/Mn-rich deposits. The three numbers represented by a point in this plot areX $_{Mn}$ ¼½Mn=Xð½$_{Fe}$Fe¼ ½þ½FeMn=ð½þð½Fe þ ½Niþ½MnCo þ ð½ÞNi10þÞ,

½CoÞ 10Þ, and X $_{NiCo}$ ¼ðð½Niþ½CoÞ10Þ=ð½Feþ½Mnþð½Niþ ½CoÞ10Þ, with [..] representing atomic percentages. The left-hand corner represents $X_{Fe} = 1$, the right-hand corner $X_{Mn} = 1$, and the top $X_{NiCo} = 1$, which implies that $X_{Fe} + X_{Mn} = 0.9$. Note that this representation works even using data normalized by [Fe]. Three types of data were compared: (1) the EMPA data for ''inner'' and ''outer'' transects (as defined in Fig. 1b and c); (2) the bulk average ICP-AES data for the 1–3 mm increments; and (3) selected literature data for the North and South Pacific Ocean (Halbach et al., 1981). Oceanic metalliferous deposits that have a high diagenetic component plot in the ''diagenetic field'' of the ternary diagram of Fig. 2 (i.e. high Mn content and a trend towards higher Ni + Co), deposits that have a hydrothermal contribution have generally low Ni + Co contents but variable Mn and Fe contents (''hydrothermal field''), and finally the ''hydrogenetic field'' contains deposits formed from seawater and they are characterized by high Ni + Co and the proportions of Mn and Fe in these deposits are relatively similar. Northern

Pacific nodules generally have a diagenetic contribution, as shown by the trend towards higher Mn/Fe and (Ni + Co)/Fe, whereas the SPG-2 nodule displays a trend toward a hydrogenetic contribution (lower Mn/Fe and (Ni + Co)/Fe content). Together with reference datasets, the SPG-2 composition indicates that it was primarily a hydrogenetic deposit throughout its growth history. This finding is consistent with the documented low flux of organic matter to the seafloor of the South Pacific Gyre (Jahnke, 1996) and reduced diagenetic contributions to the growth of the SPG-2 nodule.

3.3. Nodule morphology and trace element distributions

Backscatter scanning electron microscopy and electron microprobe analyses revealed morphological differences between ''inner'' and ''outer'' zones of the nodule (Figs. 1 and 2). In both zones, concretions with layered growth habits of two basic forms were observed: a ''botryoidal'' morphology of concentric, layered mineral growth and a porous ''matrix'' material between the botryoids. These growth habits have been previously reported (Halbach et al., 1981).

A tricolor lXRF map showing the distributions of Fe, Mn and Ni from the ''outer'' to ''inner'' zone is displayed in Fig. 3 along with a photomicrograph and the fluorescence counts for Fe, Mn and Ni along the nodule radius. A clear transition in the elemental composition was observed at approximately 12 mm: Fe increased and Mn decreased along the transect toward the nodule center. These results are consistent with the EMPA

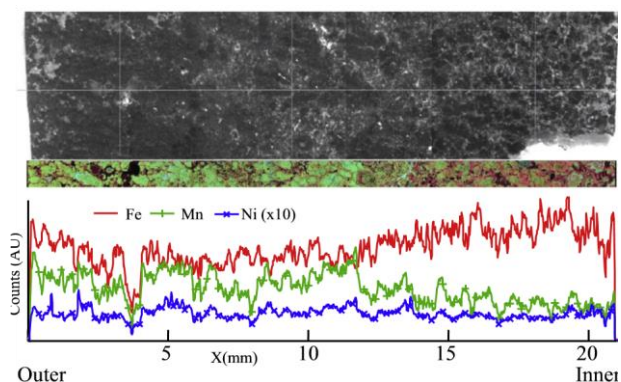Mn/Fe data (Table EA3) but not with the bulk average ICP-AES data

Fig. 3. Survey of the sample from ''outer'' (left) to ''inner'' regions. Top: Visible-light micrograph of the nodule. Middle: Tricolorcoded map showing Fe (red), Mn (green) and Ni (blue) in a strip extending from the surface of the nodule (left). Bottom: Averaged Fe, Mn and Ni counts across the map. Ni counts are multiplied by 10 relative to Mn and Fe, for clarity. The micrograph and map are to the same field of view as the plot. (For interpretation of the references to color in this figure legend, the reader is referred to the web version of this article.)

for the 1–3 mm increments. Bulk ICP-AES analyses of the 10 subsamples of the nodule do not show significant variations in metal/Fe (Table 1) across the nodule transect, suggesting uniform metal/Fe ratios in Fe and Mn-rich phases at the scale

of sampling intervals (1–3 mm). Bulk ICP-AES analyses suggest the geochemical composition of the nodule is homogenous at the bulk (1–3 mm) scale, while lXRF and EMPA data reveal a fine-scale geochemical variability along the nodule, not captured by millimeter-scale analyses.

Some trace elements, notably Ti, V and, to a lesser extent, Zn, are associated with Fe in the nodule (EMPA data; Fig. 4; V shown in Fig. 5.). Micro-XRF maps of the ''inner'' and ''outer'' zones, displayed in Fig. 5, also show this pattern. For Ti and V, the correlation with Fe is good, as viewed in red–blue bicolor maps of Fe + Ti (correlation coefficient 0.78 for ''inner'' and 0.92 for ''outer'') and Fe + V (correlation coefficient 0.86 for inner and 0.85 for outer) (Fig. 6), in which the hue is nearly uniform. Note that the Fe + Ti correlation for ''inner'' came from the same XRF map as the Fe + V correlation for ''inner'', so cover the same number of independent pixels. The same is true for the Fe + Ti and Fe + V correlations in ''outer''. Since these numbers derive from pixel-by-pixel scatterplots, it is difficult to define the number of statistically-independent points since the samples have features which are much bigger than a pixel. When Fe is shown as blue and Ti or V in red, the matrix shows slightly bluer than the ''botryoids'', indicating a slightly lower (V, Ti)/Fe ratio in the matrix than elsewhere. For Ti, the difference in ratio is about 20%, while the two types of material differ in V/Fe ratio by only 6%. The inverse correlation between Ti/Fe and Mn/Fe ratios (Fig. 4d) in the ''inner'' zone indicates that Ti is mostly
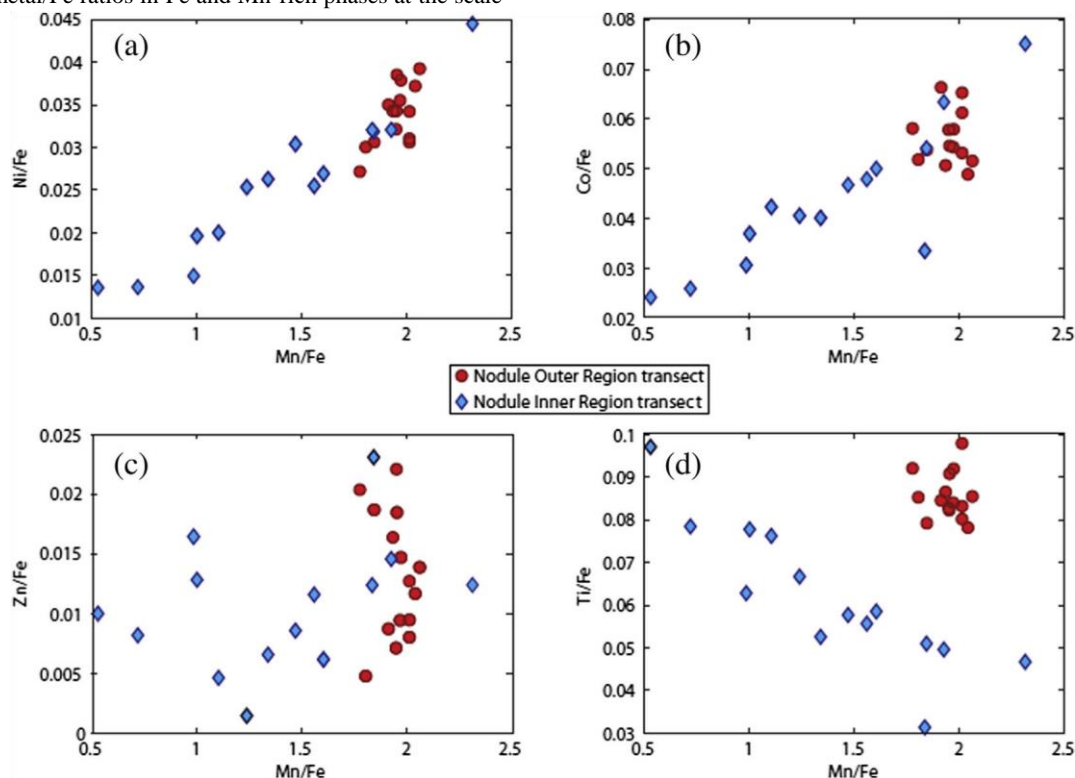

Fig. 4. Plots of Ni/Fe (A), Co/Fe (B), Zn/Fe (C) and Ti/Fe (D) ratios versus Mn/Fe ratio of electron microprobe data acquired along two transects in the nodule ''outer'' and ''inner'' regions. Position of the transects in the nodule section are shown in Fig. 1. See text for more explanation.
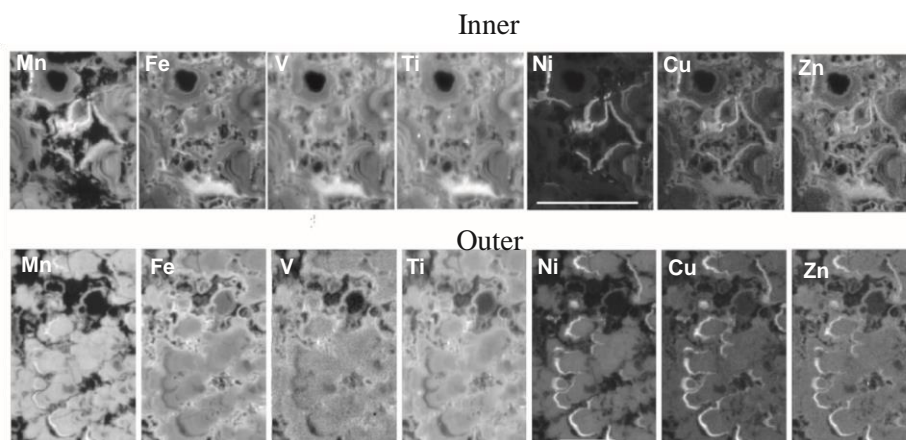
Fig. 5. lXRF maps of representative ''inner'' and ''outer'' regions showing several elements. Note that the distributions of V and Ti almost precisely match that of Fe. Zn is somewhat enriched in the matrix areas. Brighter pixels correspond to higher concentrations. Scale bars are 500 lm.
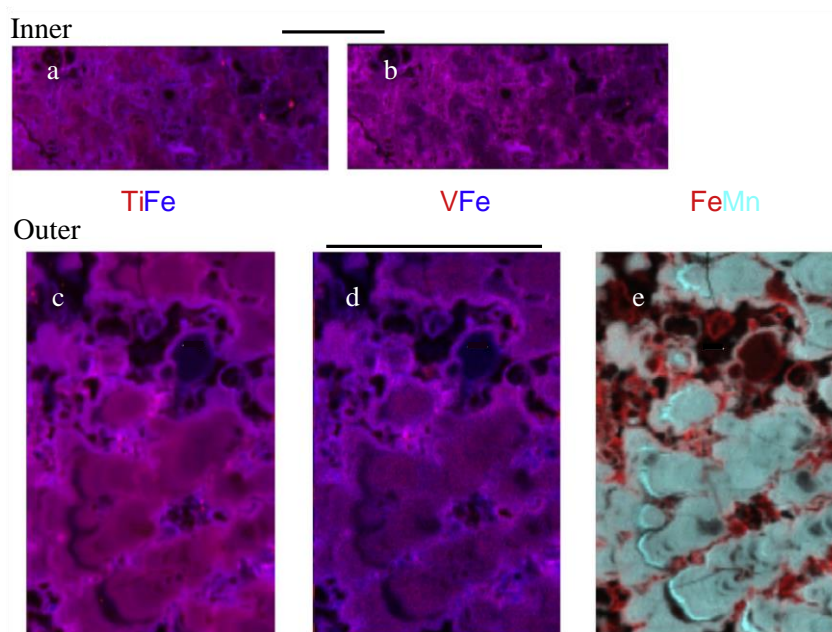

Fig. 6. Bicolor-coded maps of Ti (a,c) and V (b,d) in red, Fe in blue in ''inner'' and ''outer regions. In map (e), where Fe is shown as red and Mn as cyan, the Fe-rich ''matrix'' appears in red and the ''botryoidal'' material in shades of blue–green. Scale bars are 1 mm. (For interpretation of the references to color in this figure legend, the reader is referred to the web version of this article.)

associated with Fe. The distribution of Zn also has some features in common with that of Fe, in particular, an enrichment in the ''matrix'' areas (Fig. 5). These patterns of distribution are consistent with Ti and V bound to or incorporated in Fe-bearing mineral phases in the ''botryoids'', and Zn bound to or incorporated in Fe-bearing mineral phases in the ''matrix''.

Clear correlations in Ni/Fe and Co/Fe ratios versus Mn/ Fe suggest that Ni and Co are hosted primarily by Mn-rich minerals (Fig. 4a and b). The scatter in the Zn/Fe versus Mn/Fe data indicates that Zn may be associated with both Mn and Fe mineral phases (Fig. 4c). The lXRF data in Fig. 5 corroborate this finding by showing spatial correlation of Zn with both Fe- and Mn-rich features.

From a morphological perspective, the ''botryoidal'' features are much more pronounced in the ''outer'' zone of the nodule than in the ''inner'' zone (e.g. Fig. 5). In contrast, the Fe-rich ''matrix'' found in between the ''botryoidal'' microstructures is a more prominent morphology in the ''inner'' zone. These growth patterns, as well as the elemental composition, along the radius of the SPG-2 nodule form the basis for our definition of ''outer'' and ''inner'' zones having dominant ''botryoidal'' and ''matrix'' morphologies.

3.4. Fe-bearing phases

3.4.1. Matrix features

The EXAFS data (Fourier transform) and fits are shown in Fig. 7 along with XRF maps indicating the locations at which the spectra were taken. The data did not differ substantially among various locations within a given zone.

The Fourier transform in Fig. 7b shows the data for the ''inner'' zone locations over-plotted with a linear-combination fit using 39% feroxyhite (d-FeOOH) and 53% goethite (a-FeOOH). Although this fit is a good match to the data, it does not rule out the presence of a few percent of other species. The phase of higher-shell peaks agrees with those in the fit out to 6 Å, presumably due to the long-range order of crystalline goethite. While lXRD was not done on these specific spots, patterns taken at other matrix spots confirm the presence of goethite.

The ''matrix'' in the ''outer'' zone is typified by the spectrum and fit shown in Fig. 7a. This spectrum fits well to 28% lepidocrocite (c-FeOOH), 39% disordered biogenic oxide (Toner et al., 2009), and 18% goethite. Although the reference material we call ''biogenic oxide'' is indeed biogenic, this reference represents highly-disordered Fe oxyhydroxide from any source, biogenic or not. The XANES also fits to the same three minerals, but in proportions of 46%, 21% and 30%, respectively. However, no diffraction measurements on any spot show the strong basal (020, d = 6.26 Å) reflection expected for lepidocrocite (Fig. 8). We refer to this reflection as ''basal'' because lepidocrocite has a layered structure consisting of sheets of edge-sharing octahedra, with the conventional c-axis as the layering direction. Other lepidocrocite reflections come close enough to those from other phases such as goethite to make their identification uncertain. The basal reflection, however, is one of the strongest and should therefore appear if well-crystalline lepidocrocite were common in our samples.
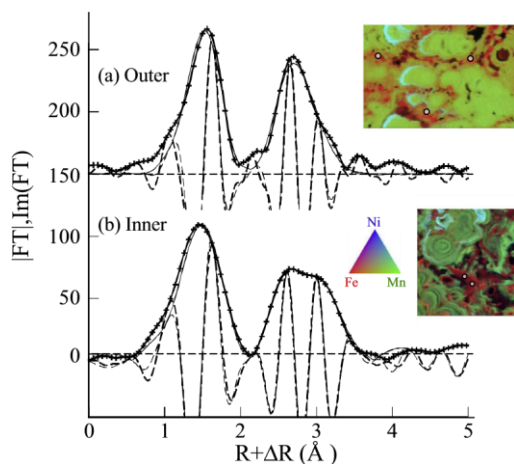

Fig. 7. EXAFS data (thick lines, symbols) and fits (thin lines) for matrix spots and corresponding tricolor maps showing location of spots at which EXAFS data were taken. The fit for the ''outer'' is a three-shell fit as discussed in text. The fit for the ''inner'' is a linear combination fit to goethite and feroxyhite. Scale bars are 200 lm. (For

interpretation of the references to colour in this figure legend, the reader is referred to the web version of this article.)
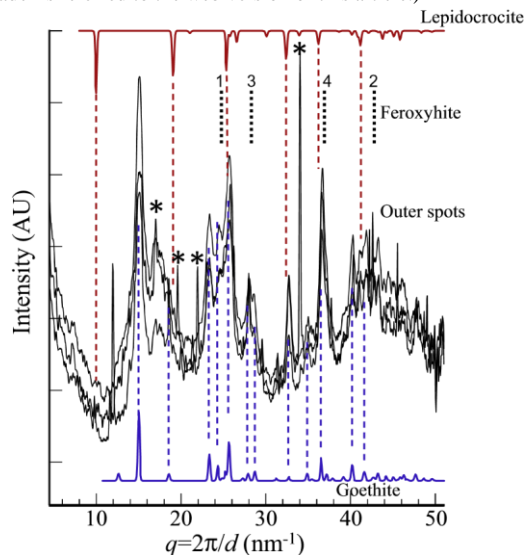

Fig. 8. Micro-XRD on ''outer matrix'' spots. Abscissa is q = 2p/d (nm[1]). The red and blue curves at top and bottom are simulated powder patterns for lepidocrocite and goethite, respectively. The red curve is flipped vertically to make it easier to trace the peak positions. The numbered peak locations for feroxyhite are from Drits et al. (1993), classified by intensity. Sharp peaks marked with asterisks match albite. (For interpretation of the references to color in this figure legend, the reader is referred to the web version of this article.)

The feature in the EXAFS spectrum, that seems to point to lepidocrocite is the prominent peak at 2.7 Å (Fig. 7a), which corresponds to edge-sharing FeO_6 octahedra. The lepidocrocite structure consists of layers of edge-sharing octahedra. The inter-layer spacing gives rise to the basal reflection, which is not found by lXRD in our samples at any spot. Thus, what the EXAFS indicates is that the material has a large fraction of edge-sharing octahedra relative to a ferrihydrite-like phase or goethite. Shell-by shell fitting yields an average Fe–O distance in the first shell of 2.01 ± 0.015 Å, an Fe–Fe shell 3.06 ± 0.03 Å with a coordination number between 2 and 6 (highly uncertain due to correlation with Dr^2), and a weak third Fe–Fe shell at 3.38 ± 0.04 Å. The coordination number of this shell is extremely uncertain due to correlation with Dr^2, but the fit is significantly better with this shell included. The Fe–Fe distances correspond nicely to edge- and cornersharing octahedra. By comparison, the edge-sharing distance in lepidocrocite is 3.067 Å and the corner-sharing distances in goethite are 3.30 Å and 3.47 Å. In addition, shells at apparent distances of 3.6 Å and 4.6 Å match those experimentally found for lepidocrocite, and correspond to Fe–Fe distances within the layers. The EXAFS evidence, and apparent lack of the lepidocrocite (002) reflection, is consistent with lepidocrocite nanoparticles that are thin in the c-direction but transversely large enough to show the high shells in EXAFS.

Note that the biogenic oxide we used as a reference material also has a relatively large ratio of edge-sharing to corner-sharing octahedra, but the overall intensity of that shell is smaller than what we find for the lepidocrocite-like material.

3.4.2. Botryoidal features

The abundance of ''botryoidal'' material varies between the ''inner'' and ''outer'' zones. Principal components analysis (PCA) of Fe EXAFS data from the spots displayed in Fig. 9 reveals a two component system. The spectra can be represented as weighted sums of signals from two materials. The first component is similar to that found for the ''inner'' matrix and is a combination of feroxyhite and goethite. The second component does not fit to a sum of our reference spectra. The nature of this component is explored below.

Spots 5 and 1 from the ''inner'' zone (Fig. 9b) are the best examples of the ''botryoidal'' Fe material. The Fourier transformed EXAFS signal for Spot 5 is shown in Fig. 10. There are strong peaks at distances similar to those found for corner- and edge-sharing octahedra. The best fit for this spectrum contains four contributions. One is an Fe–O shell represented as the Fe–O first neighbor from feroxyhite. While the Fe–O shell is actually split, the data do not cover a long enough k-range to resolve this splitting, and the first shells of our models are well-represented as single shells. Next is a Fe–Fe shell at 3.04 ± 0.038 Å with a coordination number (CN) of 2.3–9. The distance found for this shell is consistent with edge-sharing octahedra such as those found in lepidocrocite (3.06 Å), whose edge-sharing peak was used as an experimental reference. This contribution requires an additional mean-square relative displacement (MSRD, second moment of the distance distribution) of 0.014– 0.047 Å ^{2}, beyond that found in lepidocrocite. This is a significant dispersion, which may reflect

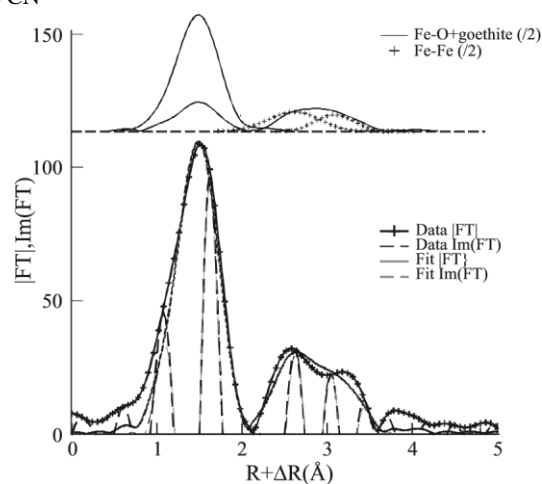an unresolved splitting. The large error bars on this number and the CN

Fig. 10. Fit of Inner spot 5 (see bottom panel of Fig. 9) to Fe–O, two Fe–Fe shells and goethite. The top panel shows the contributions of each shell (divided by 2). The bottom panel shows the magnitude and imaginary parts of the FT for data and fit.

reflect parameter correlation between the two. It was found necessary to add a contribution from goethite, which was used without any adjustment except for amount and included all shells out to 3.5 Å . The result showed that 10–25% of the Fe in the sample had to be assumed to be in the form of goethite, though it is possible that some of the other oxides would provide an acceptable fit in this role. Note that the coordination numbers quoted above and below for non-goethite Fe–Fe shells is the average over all Fe atoms; they should be divided by ''1-(goethite fraction)'' to get the Fe–Fe CNs in the 75–90%
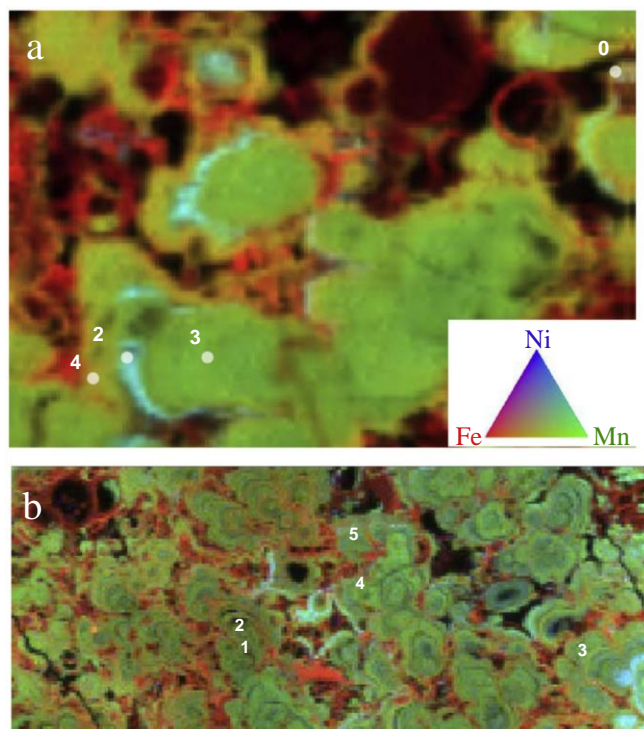

g. 9. Tricolor-coded lXRF maps showing botryoidal spots on which spectroscopy was performed in ''outer'' (a) and ''inner'' (b) regions. Scale bars e 200 lm (a) and 800 lm (b).

of the spot 5 material that is not goethite. A fit with only these three contributions always showed a discrepancy in the FT at around 3.3 Å (apparent). While the phase would match, the amplitude did not. To solve this problem, an additional Fe–Fe shell at $3.45 \pm .0.04$ Å (CN 0.25–0.9) was added to the fit. This distance is comparable to the longer corner-sharing distance in goethite (3.47 Å), thus we interpret it as coming from corner-sharing octahedra in the non-goethite fraction. The MSRD of this shell was assumed to be the same as that in the reference lepidocrocite edge-sharing shell, in order to reduce the number of free parameters. To summarize, the three contributions we find to the Fe environment are goethite, edge-sharing octahedra as in lepidocrocite, and a smaller number of corner-sharing octahedra. We were not able to identify the exact minerals containing these coordination polyhedra (except goethite).

The result of fitting is shown in the bottom panel of Fig. 10, as the FT magnitude and imaginary part of the data compared with the fit, along with the FT magnitudes of the individual components in the top panel of Fig. 10.

3.5. Valence states of Ti and V

For Ti, three XANES spectra were taken at ''matrix'' points from within the ''outer'' zone. Titanium EXAFS was not possible due to the interference of the Ba L_3 edge, about 280 eV above the Ti K-edge. The best match between the data and references was ilmenite ($FeTiO_3$), as shown in Fig. 11. The match is not perfect; therefore, the Ti phase within the SPG-2 ''outer'' ''matrix'' is not literally ilmenite. Rather, the Ti is likely tetravalent and in octahedral coordination to oxygen which share edges with FeO_6 octahedra: as in the ilmenite structure. Since the ''matrix'' is largely composed of goethite, which consists of edge-sharing Fe–O octahedra, it is plausible

that the spectrum could be accounted for by Ti sorbed to or substituted within goethite.

Vanadium XANES spectra for points from the ''inner matrix'', ''inner botryoid'', and ''outer botryoid'' regions were collected. All of these spectra fit with a twocomponent model generated by Iterative Target Factor Analysis (ITFA). These two component spectra, ITFA0 and ITFA1, are shown in Fig. 12 along with spectra for V(V) sorbed to 2-line ferrihydrite and d-MnO_2. Note that the pre-edge peak intensity is lower for d-MnO_2-sorbed V than for ferrihydrite-sorbed V. Although the pre-peak height is often taken as a sign of valence state, both standards are pentavalent, and the difference is presumably due to the differing symmetry of the V site (Wong et al., 1984; Tanaka et al., 1987).

Fig. 13 shows a trend in the V speciation as a function of the local Fe/Mn ratio. The use of the logarithm as the abscissa is not meant to imply any theory; it is for plotting convenience only. In order to understand the trend, an analysis of the V spectral end-members was attempted. Fig. 14 displays fits of ITFA-derived end-member spectra to a combination of V-sorbed standards and, for ITFA0, $LaCl_3 7H_2O$, which is needed to represent a small amount of La, whose intense white line makes for a sharp peak at 5489 eV. Vanadium-sorbed goethite (two loadings) and hematite standards did not appear in the fits to either ITFA component. Component ITFA0, which is most prominent in Mn-rich regions, is well-represented by a mixture of the two sorbed standards (29% Mn, 66% Fe, 4% La), suggesting that V is hosted by the nanoparticulate oxides which form the bulk of the nodule. However, ITFA1, which is found in Fe-rich regions, does not fit well. The best fit is to V on d-MnO_2 alone, which seems odd as there is little Mn in the areas in which ITFA1 is most prominent. In addition, the fit quality is not nearly as good as for ITFA0. It is possible to improve the fit by adding such species as VO_2 and V_2O_5, but it is probable that such a combination merely reconstructs the spectrum without representing the
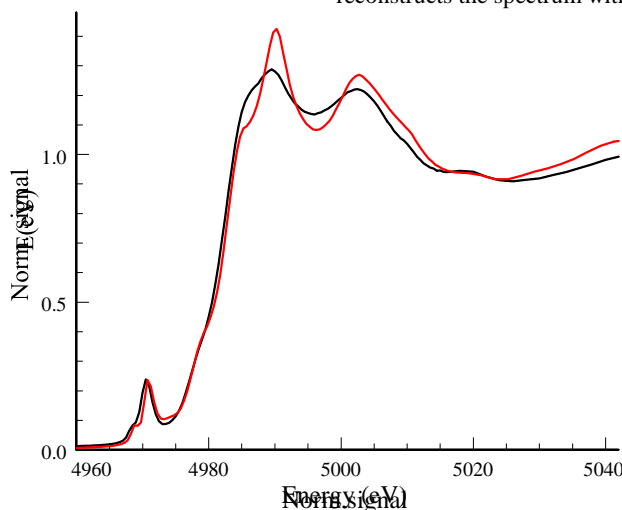

Fig. 11. XANES for Ti in ''inner'' matrix (average of 3 spots, black) compared with that of ilmenite (red). (For interpretation of the references to color in this figure legend, the reader is referred to the web version of this article.)
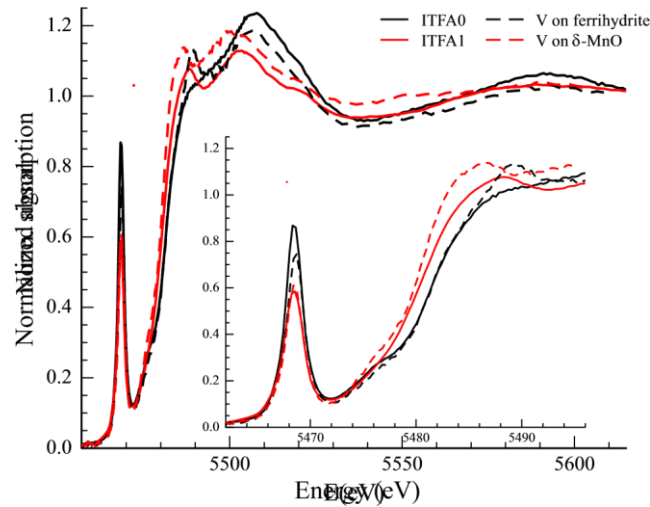
Fig. 12. V K-XANES spectra for the ITFA end-members found in the nodule (solid black, solid red), V(V) on 2-line ferrihydrite (dashed black), and V(IV) on d-MnO$_2$ (dashed red). The inset shows the pre-edge region on an expanded scale. (For interpretation of the references to color in this figure legend, the reader is referred to the web version of this article.)
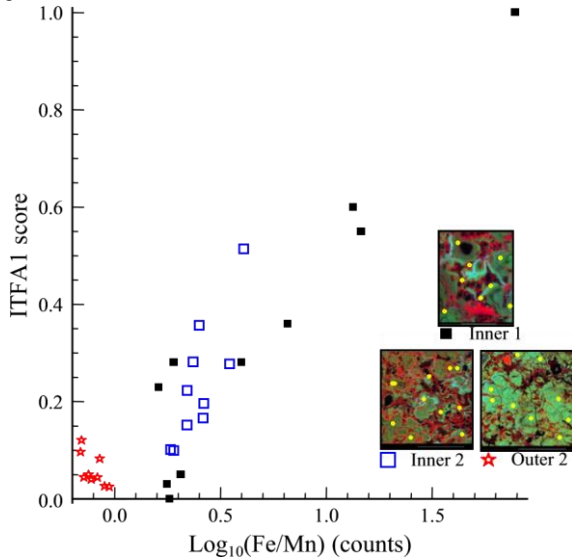

Fig. 13. Correlation between fitted fraction of ITFA1 end-member and the ratio of counts in the Fe to Mn XRF channels. Small tricolor (red = Fe, green = Mn, blue = Ni) maps show where points were taken. Maps Inner2 and Outer2 were taken in the same run on the same thin-section; map Inner1 came from a different run and thin section. Map Inner1 is 777 lm tall; maps Inner2 and Outer2 are 2000 lm tall. (For interpretation of the references to color in this figure legend, the reader is referred to the web version of this article.)

true V species. This is a common challenge with databasedriven data fitting; the true species is likely something missing from our database. If V were to be co-deposited in or sorbed on Fe oxyhydroxide in octahedral symmetry, it might also have a low pre-edge peak. Therefore, the ITFA1 species is tentatively assigned to V in octahedral coordination to oxygen and sorbed to Fe oxyhydroxides. It should be noted that an ITFA end-member may easily be a mixture of actual species as the fit proved true in the case of the ITFA0 discussed above.

3.6. Fe isotope composition

Iron isotope composition along the nodule section yields a range of values from 0.16 to 0.07 ± 0.09‰ (2sd; Table 1). The d$^{56/54}$Fe values are constant within uncertainty along the nodule radius with an average value of 0.12 ± 0.07‰ (2sd) for the 10 increments analyzed. This means that constant Fe isotope values, when averaged over 1–3 mm increments or approximately 0.25–0.74 Ma intervals, were observed over a period of 4 Ma. We observe that Fe in the ''inner'' part of the nodule is isotopically identical to Fe present in the ''outer'' part. Although our measurement interval is too coarse to resolve the isotopic signature of Fe-rich ''matrix'' versus Mn-rich botryoidal structures, our results are consistent with similar isotope values for ''matrix'' and ''botryoids'' because there is more ''matrix'' in the ''inner'' part and more ''botryoids'' in the ''outer'' part of the nodule, yet the isotope values are the same within experimental error. Moreover, the Fe isotopes recorded in the SPG-2 nodule are within the range of Fe isotope compositions reported for slowly precipitated hydrogenetic ferromanganese crusts (1.2 to +1.6‰) (Zhu et al., 2000; Levasseur et al., 2004; Chu et al., 2006; Horner et al., 2015).

4. DISCUSSION

4.1. Mineral structure and stability

Our results indicate that the Fe speciation in the hydrogenetic South Pacific Gyre nodule is considerably more complex than expected and quite different from the uniform amorphous FeOOH ''background'' component typically discussed in the literature. Iron oxyhydroxides in
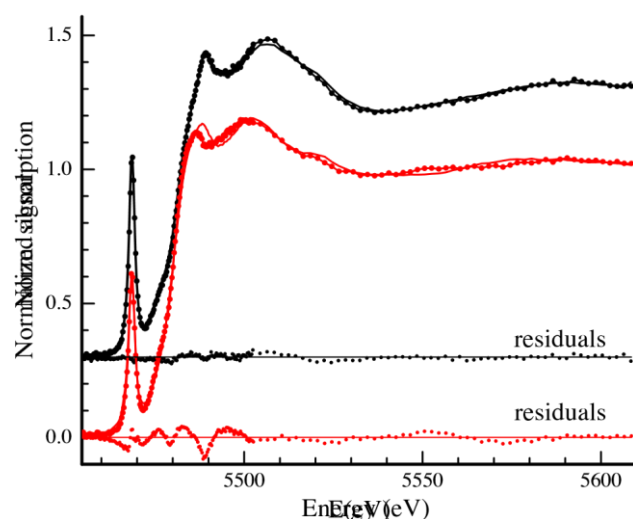
Fig. 14. Fits of the ITFA0 (black) and ITFA1 (red) end-members to d-MnO$_2$-sorbed V, 2-line ferrihydrite-sorbed V and LaCl$_3$7H$_2$O. Data and residuals are shown in points and fits in solid lines. (For interpretation of the references to color in this figure legend, the reader is referred to the web version of this article.)

the SPG-2 nodule are present in a wide variety of forms – goethite (a-FeOOH), goethite polymorphs feroxyhite (d^0-FeOOH) and nano-lepidocrocite (c-FeOOH), and biogenic-like ferrihydrite. Each of these phases is thought to form under different environmental conditions (pH and Eh, as examples). Therefore, although the SPG-2 nodule formed in a well-oxygenated environment, the diversity of phases observed should reflect either changes in the deepsea environment at the sediment–water interface or mineral transformation processes over 3.65–4.05 Ma of growth (Schwertmann and Cornell, 2000).

The major trend in Fe speciation within the ''matrix'' material is a positive correlation between the abundance of stable Fe oxyhydroxides (goethite) and age of deposition. Specifically, Fe EXAFS data reveal that goethite is more abundant in the ''inner'' (older) deposits than in the ''outer'' (younger) deposits, 53 mol% and 18 mol%, respectively. Therefore, the SPG-2 nodule hosts a series of phases in which the mineral stability of the Fe oxyhydroxides increases with the age of the deposit.

The ''outer matrix'' consists of goethite < lepidocrocite < biogenic-like ferrihydrite. Approximately 1/3 of the ''outer matrix'' is a c-disordered lepidocrocite. Lepidocrocite is typically observed in low oxygen environments with Fe^{2+} present, and is meta-stable with respect to goethite (Schwertmann and Cornell, 2000). In general, the ''outer matrix'' is characterized by poorly-crystalline Fe oxyhydroxide phases consistent with those observed in modern low-temperature, deep-sea deposits where microbial activity is evident (Toner et al., 2009, 2012). However, microbial activity is not a necessary condition for the precipitation of poorly-crystalline phases. For example, strongly sorbing ligands such as P, Si, and As produce Fe(III) precipitates with these characteristics, and transition metal impurities are known to slow recrystallization processes (Cornell et al., 1992). The

structural characteristics and abundance of meta-stable phases suggests that the younger nodule deposits precipitated in the presence of: (1) Fe^{2+} (lepidocrocite-like phase), or (2) metals, ligands, or under the influence of biology (biogenic-like ferrihydrite).

The ''inner matrix'', can be understood as a mixture of two FeOOH polymorphs, feroxyhite and goethite. In the laboratory, feroxyhite is a meta-stable phase generated by very rapid oxidation of Fe^{2+} in alkaline medium (Chukhrov et al., 1977). In the field, feroxyhite is observed in the pore spaces of sediments hosting Fe^{2+}-rich waters (Carlson and Schwertmann, 1980). In poorly drained soils, where ferrihydrite, lepidocrocite, goethite, and feroxyhite are observed within the profile, feroxyhite is associated with the Mn oxide vernadite (Birnie and Paterson, 1991). While the conditions of feroxyhite formation in laboratory and field studies are consistent with one another and with what we know of the SPG-2 nodule – precipitation in pore spaces near Mn-rich phases – there is little consensus in early literature regarding the stability relationship between feroxyhite and goethite. Chukhrov et al. (1977) proposed that feroxyhite is meta-stable with respect to goethite. However, Carlson and Schwertmann (1980) concluded that feroxyhite does not recrystallize to form goethite, but that the two phases form under different conditions, namely fast oxidation of Fe^{2+} (feroxyhite) versus slow precipitation of Fe^{3+} (goethite). More recently, the stability, and transformation time, for pure oxyhydroxides with respect to hematite in the presence of trace Fe^{2+} was established as: ferrihydrite 6 feroxyhite < lepidocrocite < akaganeite << goethite (Lu et al., 2011). In agreement with Lu et al., when particle size and mineral surface hydration are considered, goethite was most often the stable phase relative to coarse hematite over a wide range of surface area/particle size conditions; however, at high surface area values ferrihydrite can be the stable phase (Navrotsky et al., 2008). These results may indicate that feroxyhite precipitated from a sediment source (fast oxidation of Fe^{2+}), while goethite precipitated in contact with ambient seawater (slow precipitation of Fe^{3+}). In this conceptual framework, the presence of feroxyhite would reflect the

"diagenetic" source of metals (sediment porewaters), while goethite would be indicative of the "hydrogenetic" source of metals (seawater dissolved trace metals).

Iron minerals with a known role for Fe^{2+} (aq) in their formation were observed in both the "inner" and "outer" matrix materials, feroxyhite and lepidocrocite, respectively. Given the overall hydrogenetic character of the nodule and the low biological productivity of the overlying waters, we do not have a good explanation for a source of Fe^{2+} (aq) or the presence of these minerals. While Fe is abundant in this depositional environment, our understanding of the seafloor conditions points to low availability of Fe^{2+} (aq). Two possible explanations for the presence of Fe^{2+} (aq) should be considered. First, the overall hydrogenetic character of the nodule does not rule out all contributions of material from the sediments. Second, even in low productivity waters there may be enough organic material delivered to the seafloor to promote some Fe reduction during the deposition of the "matrix" materials. We must conclude that either a very low supply of Fe^{2+} (aq) is sufficient to influence the mineralogy of these slowly accumulating deposits or that the presence of lepidocrocite and feroxyhite do not indicate an Fe^{2+} (aq) precursor.

The "botryoidal" material is a combination of crystalline minerals similar to those found in the "matrix", plus another material whose most distinctive feature is the presence of edge-sharing octahedra with considerable dispersion in Fe–Fe distance. In the "botryoidal" microstructures, as opposed to the "matrix", there is considerable Mn in addition to the Fe. Thus, the possibility should be considered that we have a mixed phase in which the nearest cation neighbor to Fe is not always Fe but is sometimes Mn, such as in "Fe-vernadite". However, the "botryoidal" material need not be a single phase, and could include Fe-rich and Mn-rich material too finely intergrown to have been resolved in this study. If the two phases have differing Fe–Fe distances, then the resulting average EXAFS could show a large MSRD. However, because linearcombination fitting did not produce a match, at least one of these phases must be something not found in our spectral database. Consistent with intergrowth between Mn and Fe minerals, the "botryoidal" material includes several percent of other transition metals such as Cu, Ni, Co and Zn, which are known to be associated primarily with Mn oxide minerals in hydrogenetic ferromanganese crusts (Halbach and Puteanus, 1984; Koschinsky and Halbach, 1995; Koschinsky et al., 1997; Hein et al., 2003; Koschinsky and Hein, 2003).

4.2. Trace element association with Fe oxyhydroxides

For the SPG-2 nodule, trace element distributions and speciation were determined by lXRF mapping and lXANES, respectively. Trace elements Ti and V were colocated with the Fe-rich "matrix" materials of the "inner" and "outer" nodule. In contrast, transition metals Ni, Cu, and Zn are primarily co-located with Mn within the "botryoidal" materials of the "inner" and "outer" nodule. These observations are consistent with a vast literature base demonstrating the affinity of oxyanions such as V for Fe oxyhydroxide minerals, and the affinity of divalent

cations for Mn oxide minerals, in laboratory experiments and field observations (Nicholson and Eley, 1997; Brown et al., 1999; Cornell and Schwertmann, 2003). More specifically, our lXRF and lXAS observations build on previous investigations of hydrogenetic deposits that employed operationally defined, wet-chemical approaches. A strong correlation between Co, Ni, Cd, Zn, Cu and Mn in a "d-MnO$_2$" phase was observed in hydroxylamine hydrochloride leaching experiments (Koschinsky and Halbach, 1995). Similarly, Ti and V were correlated with an "amorphous FeOOH" phase that dissolved in the presence of oxalic acid (Koschinsky and Halbach, 1995). Our X-ray microprobe observations confirm the interpretation of leaching experiments by showing that Ti and V are co-located with the Fe phases of the "matrix" throughout the SPG-2 nodule. In addition to co-location, Ti and V XANES results are most consistent with tetravalent Ti and pentavalent V in octahedral coordination to oxygen and adsorbed to Fe oxyhydroxides in the nodule. These associations did not vary along the growth radius of the nodule. Considering the evidence for mineral alteration over time, our Ti and V data indicate that trace metal speciation within the nodule is not over-written or erased as the minerals age to more stable phases.

Looking at the difference between "inner" and "outer" regions, we see that the Ti/Fe ratio (Tables EA1 and EA2) decreases on going from "outer" to "inner", and the difference between the Ti/Fe ratio in matrix vs. botryoids increases. We speculate that as the Fe minerals age and become more crystalline, Ti is expelled from surface or edge sites. This effect would depend on which Fe minerals are involved, so might be expected to differ between matrix and botryoidal material. An analogous effect has been seen for Ni in the goethite fraction of lateritic soil by Dublet et al. (2015).

4.3. Fe isotope composition along the nodule

The biogeochemical cycling of Fe in the oceans has important implications for the biological pump because Fe is a bio-limiting nutrient (Martin and Fitzwater, 1988). Thus, Fe bioavailability in marine environments through time could have influenced the regulation of the carbon cycle. Iron is delivered to the oceans from continents by rivers, glaciers, and windblown particles (dust), as well as by release from continental shelf sediments and hydrothermal venting (Raiswell and Canfield, 2012). These sources of Fe have different d$^{56/54}$Fe values that are further modified by chemical processes in the ocean (Beard et al., 2003; Chu et al., 2006; Dauphas and Rouxel, 2006; Severmann et al., 2010; Radic et al., 2011; John et al., 2012; Conway and John, 2014; Scholz et al., 2014; Horner et al., 2015). Hence, temporal Fe isotope variations in seawater, as recorded by ferromanganese hydrogenetic deposits, may help deciphering the variability of Fe sources to the oceans (Zhu et al., 2000; Chu et al., 2006; Horner et al., 2015). For instance, the Fe isotope composition in a Pacific hydrogenetic ferromanganese crust over 76 Ma shows that deep Fe sources (e.g. hydrothermal Fe) may have strongly influenced the Fe supply to the oceans over the Cenozoic (Horner et al., 2015). These findings questioned the

general assumption that aeolian dust particles are the predominant source controlling the biogeochemical cycling of Fe in modern oceans. However, because precipitation and adsorption processes as well as mineralogy can fractionate Fe isotopes, our study provides a framework for understanding the relationships between fine-scale mineralogical variability in a ferromanganese nodule and preservation of Fe isotope composition from seawater.

The elemental composition for the nodule determined through bulk and micro-probe measurements, is typical of that reported for deep-sea hydrogenetic manganese nodules (Hein et al., 2013) and indicates that the source of metals to the nodule were from seawater sources, rather than sediments, during the time span we investigated. Fe isotope variations should be controlled by either changes in seawater Fe isotope composition, or by geochemical processes occurring in the nodule. The two main possible causes for fine-scale Fe isotope variability are the diffusion of Fe throughout the nodule and from seawater, and isotopic fractionation during exchange reactions and alteration to more stable phases associated with sorption reactions.

Based on a calculated diffusion coefficient for the nodule ($<1.10^{12}$ cm^2/year) (Henderson and Burton, 1999), we suggest that diffusion of Fe from seawater to the nodule cannot explain the homogeneous d$^{56/54}$Fe pattern. Our results rule out the effect of mineral alteration as a cause of measurable Fe isotopic fractionation. As discussed above, we did observe changes in the nodule mineralogy as well as variations in Fe contents and Mn/Fe ratios, as shown by lXRF and EMPA transects data in Figs. 1–3, which could potentially have altered the original distribution of Fe isotopes along the nodule. However, while the Fe minerals in the nodule altered to more stable phases over time, the Fe isotope composition, on a 2–3 mm sampling scale along the radius of growth, remained constant throughout the nodule (0.12 ± 0.07‰). Despite a range of Fe isotope fractionation factors that were measured during laboratory experiments involving adsorption reactions and scavenging on Fe-phases (e.g. (Bullen et al., 2001; Skulan et al., 2002; Johnson et al., 2005; Wu et al., 2011)), Horner et al. (2015) report that the isotopic fractionation caused by the precipitation of dissolved seawater Fe (most likely in the form of Fe(III)-ligand) to hydrogenetic ferromanganese crusts is D$^{56/54}$Fe $= +0.77 \pm 0.06$‰. If we apply this fractionation factor, D$^{56/54}$Fe(seawater– nodule) $=$ d$^{56/54}$Fe(seawater) d$^{56/54}$Fe(nodule), to our hydrogenetic nodule, then we obtain a d$^{56/54}$Fe source value of $+0.65$‰ which is consistent with dissolved Fe dominated by dust dissolution as reported in the Atlantic Ocean (e.g. $+0.70 \pm 0.01$‰; (Conway and John, 2014)). Finally, implementation of our analytical approach to different type of nodules (e.g. including nodules with a high diagenetic imprint) will help addressing the issue of the influence of the nature of precursor Fe-phases on the fractionation of Fe isotopes during sorption reactions and scavenging.

5. CONCLUSIONS

Our results provide a framework for addressing the degree to which deep-sea ferromanganese nodules are archives of past oceanic conditions through trace element uptake and preservation of chemical and isotopic features over time. First, in the Fe mineralogy, we observe a transition from a low abundance of goethite in the ''outer matrix'' to higher abundance in the ''inner matrix'' that is consistent with transformation of lepidocrocite- and ferrihydrite-like phases to goethite over time. From these observations, we propose that the incipient Fe ''matrix'' is composed of poorly ordered ferrihydrite and lepidocrocite phases. The initial trace element uptake signatures should then be determined by the characteristics of the incipient phases and the composition of the seawater at the sediment–water interface. As these phases are buried within the nodule by subsequent mineral growth at the nodule surface, we observe evidence for mineral transformation. Despite mineral transformation to more stable phases, the Ti and V coordination chemistry and Fe stable isotope signatures are consistent along the growth radius of the SPG-2 nodule. These observations indicate that while the Fe mineral phases within nodules do undergo alteration to more stable phases, the trace element speciation (with Ti and V as examples) and Fe isotope composition do not change in response. The primary implication of these findings is that buried layers of nodules are out of contact—geochemi cally—with surrounding seawater. Therefore, we conclude that the Fe minerals in MFNs are indeed faithful recorders of trace elements, at least Ti and V, over time.

APPENDIX A. SUPPLEMENTARY DATA

Supplementary data associated with this article can be found, in the online version, at http://dx.doi.org/10.1016/j.gca.2015.08.021.

REFERENCES

Albare`de F. and Beard B. (2004) Analytical methods for nontraditional isotopes. Rev. Mineral. Geochem. 55, 113–152.

Aplin A. C. and Cronan D. S. (1985) Ferromanganese oxide deposits from the Central Pacific Ocean, II. Nodules and associated sediments. Geochim. Cosmochim. Acta 49, 437–451.

Axelsson M. D., Rodushkin I., Ingri J. and Ohlander B. (2002) Multielemental analysis of Mn–Fe nodules by ICP-MS: optimisation of analytical method. Analyst 127, 76–82.

Banakar V. K. and Tarkian M. (1991) Genesis and growth of internal microstructures of manganese nodules. Indian J. Mar. Sci. 20, 20–24.

Banerjee R., Roy S., Dasgupta S., Mukhopadhyay S. and Miura H. (1999) Petrogenesis of ferromanganese nodules from east of the Chagos Archipelago, Central Indian Basin, Indian Ocean. Mar. Geol. 157, 145–158.

Baturin G. N. and Savenko V. S. (1989) Growth rates of deepwater iron–manganese nodules. Oceanology 29, 334–342.

Beard B. L., Johnson C. M., Von Damm K. L. and Poulson R. L. (2003) Iron isotope constraints on Fe cycling and mass balance in oxygenated Earth oceans. Geology 31, 629–632.

Bhat S., Krishnaswami S., Lal D., Rama D. and Somayajulu B. (1973) Radiometric and trace element studies of ferromanganese nodules. Proc. Symp. Hydrogeochem. Biogeochem., 443– 462.

Birnie A. C. and Paterson E. (1991) The mineralogy and morphology of iron and manganese oxides in an imperfectlydrained Scottish soil. Geoderma 50, 219–237.

Bonatti E., Kraemer T. and Rydell H. (1972) Classification and genesis of submarine iron-manganese deposits. In Ferromanganese deposits on the Ocean Floor (ed. D. Horn). Nat. Sci. Found., Washington, DC, pp. 149–165.

Brown, Jr., G. E., Henrich V. E., Casey W. H., Clark D. L., Eggleston C., Felmy A., Goodman D. W., Gratzel M., Maciel G., McCarthy M. I., Nealson K. H., Sverjensky D. A., Toney M. F. and Zachara J. M. (1999) Metal oxide surfaces and their interactions with aqueous solutions and microbial organisms. Chem. Rev. 99, 77–174.

Bullen T. D., White A. F., Childs C. W., Vivit D. V. and Schulz M. S. (2001) Demonstration of significant abiotic iron isotope fractionation in nature. Geology 29, 699–702.

Calvert S. E. and Cronan D. S. (1978) Geochemistry of oceanic ferromanganese deposits. Philos. Trans. R. Soc. Lond. A 290, 43–73.

Carlson L. and Schwertmann U. (1980) Natural occurrence of feroxyhite (d'-FeOOH). Clays Clay Miner. 28, 272–280.

Chmeleff J., von Blanckenburg F., Kossert K. and Jakob D. (2010) Determination of the ^{10}Be half-life by multicollector ICP-MS and liquid scintillation counting. Nucl. Instrum. Methods Phys. Res., Sect. B 268, 192–199.

Chu N.-C., Johnson C., Beard B., German C., Nesbitt R., Frank M., Bohn M., Kubik P., Usui A. and Graham I. (2006) Evidence for hydrothermal venting in Fe isotope compositions of the deep Pacific Ocean through time. Earth Planet. Sci. Lett. 245, 202–217.

Chukhrov F., Zvyagin B., Gorshkov A., Yermilova L., Korovushkin V., Rudnitskaya Y. S. and Yakubovskaya N. Y. (1977) Feroxyhyte, a new modification of FeOOH. Int. Geol. Rev. 19, 873–890.

Conway T. M. and John S. G. (2014) Quantification of dissolved iron sources to the North Atlantic Ocean. Nature 511, 212–215. Cornell R. M. and Schwertmann U. (2003) The Iron Oxides: Structure, properties, Reactions, Occurrences and Uses, second, completely revised and extended ed. Wiley-VCH, Darmstadt, Germany.

Cornell R. M., Giovanoli R. and Schneider W. (1992) The effect of nickel on the conversion of amorphous iron(III) hydroxide into more crystalline iron oxides in alkaline media. J. Chem. Technol. Biotechnol. 53, 73–79.

Cronan D. S. (1975) Manganese nodules and other ferromanganese oxide deposits from Atlantic Ocean. J. Geophys. Res. Oceans Atmos. 80, 3831–3837.

Dauphas N. and Rouxel O. (2006) Mass spectrometry and natural variations of iron isotopes. Mass Spectrom. Rev. 25, 515–550.

de Lange G. J., van Os B. and Poorter R. (1992) Geochemical composition and inferred accretion rates of sediments and manganese nodules from a submarine hill in the Madeira Abyssal Plain, eastern North Atlantic. Mar. Geol. 109, 171–194.

D'Hondt S., Spivack A. J., Pockalny R., Ferdelman T. G., Fischer J. P., Kallmeyer J., Abrams L. J., Smith D. C., Graham D., Hasiuk F., Schrum H. and Stancin A. M. (2009) Subseafloor sedimentary life in the South Pacific Gyre. Proc. Natl. Acad. Sci. 106, 11651–11656.

Dideriksen K., Baker J. A. and Stipp S. L. S. (2006) Iron isotopes in natural carbonate minerals determined by MC-ICP-MS with a Fe-58-Fe-54 double spike. Geochim. Cosmochim. Acta 70, 118–132.

Drits V., Sakharov B. and Manceau A. (1993) Structure of feroxyhite as determined by simulation of X-ray diffraction curves. Clay Miner. 28, 209-209.

Dublet G., Juillot F., Morin G., Fritsch E., Fandeur D. and Brown G. E. (2015) Goethite aging explains Ni depletion in upper units of ultramafic lateritic ores from New Caledonia. Geochim. Cosmochim. Acta 160, 1–15.

Dymond J., Lyle M. W., Finney B., Piper D. Z., Murphy K., Conard R. and Pisias N. (1984) Ferromanganese nodules from MANOP Sites H, S, and R – control of mineralogical and chemical composition by multiple accretionary processes. Geochim. Cosmochim. Acta 48, 931–949.

Ebert K., Willenbring J., Norton K. P., Hall A. and Ha¨ttestrand C. (2012) Meteoric ^{10}Be concentrations from saprolite and till in northern Sweden: implications for glacial erosion and age. Quat. Geochronol. 12, 11–22.

Eickhoff M., Obst M., Schro¨der C., Hitchcock A. P., Tyliszczak T., Martinez R. E., Robbins L. J., Konhauser K. O. and Kappler A. (2014) Nickel partitioning in biogenic and abiogenic ferrihydrite: the influence of silica and implications for ancient environments. Geochim. Cosmochim. Acta 140, 65–79.

Elderfield H., Hawkesworth C. J., Greaves M. J. and Calvert S. E. (1981) Rare-earth element zonation in Pacific ferromanganese nodules. Geochim. Cosmochim. Acta 45, 1231–1234.

Frierdich A. J. and Catalano J. G. (2012) Controls on Fe(II)activated trace element release from goethite and hematite. Environ. Sci. Technol. 46, 1519–1526.

Frierdich A. J., Luo Y. and Catalano J. G. (2011) Trace element cycling through iron oxide minerals during redox-driven dynamic recrystallization. Geology 39, 1083–1086.

Gradstein F. and Ogg J. (2002) Future directions in stratigraphy. Episodes 25, 203–208.

Graham I., Carter R., Ditchburn R. and Zondervan A. (2004) Chronostratigraphy of ODP 181, Site 1121 sediment core (Southwest Pacific Ocean), using ^{10}Be/^{9}Be dating of entrapped ferromanganese nodules. Mar. Geol. 205, 227–247.

Halbach P. and Puteanus D. (1984) The influence of the carbonate dissolution rate on the growth and composition of Co-rich ferromanganese crusts from Central Pacific seamount areas. Earth Planet. Sci. Lett. 68, 73–87.

Halbach P., Scherhag C., Hebisch U. and Marchig V. (1981) Geochemical and mineralogical control of different genetic types of deep-sea nodules from the Pacific Ocean. Miner. Deposita 16, 59–84.

Hammersley A. (1997) FIT2D: an introduction and overview. European Synchrotron Radiation Facility Internal Report ESRF97HA02T.

Heggie D., Kahn D. and Fischer K. (1986) Trace metals in metalliferous sediments, MANOP Site M: interfacial pore water profiles. Earth Planet. Sci. Lett. 80, 106–116.

Hein J. R., Koschinsky A. and Halliday A. N. (2003) Global occurrence of tellurium-rich ferromanganese crusts and a model for the enrichment of tellurium. Geochim. Cosmochim. Acta 67, 1117–1127.

Hein J. R., Mizell K., Koschinsky A. and Conrad T. A. (2013) Deep-ocean mineral deposits as a source of critical metals for high- and green-technology applications: comparison with land-based resources. Ore Geol. Rev. 51, 1–14.

Henderson G. M. and Burton K. W. (1999) Using (^{234}U/^{238}U) to assess diffusion rates of isotope tracers in ferromanganese crusts. Earth Planet. Sci. Lett. 170, 169–179.

Horner T. J., Williams H. M., Hein J. R., Saito M. A., Burton K. W., Halliday A. N. and Nielsen S. G. (2015) Persistence of deeply sourced iron in the Pacific Ocean. Proc. Natl. Acad. Sci., 201420188.

Jahnke R. A. (1996) The global ocean flux of particulate organic carbon: areal distribution and magnitude. Global Biogeochem. Cycles 10, 71–88.

John S. G., Mendez J., Moffett J. and Adkins J. (2012) The flux of iron and iron isotopes from San Pedro Basin sediments. Geochim. Cosmochim. Acta 93, 14–29.

Johnson C. M., Roden E. E., Welch S. A. and Beard B. L. (2005) Experimental constraints on Fe isotope fractionation during magnetite and Fe carbonate formation coupled to dissimilatory hydrous ferric oxide reduction. Geochim. Cosmochim. Acta 69, 963–993.

Klinkhammer G., Heggie D. T. and Graham D. W. (1982) Metal diagenesis in oxic marine-sediments. Earth Planet. Sci. Lett. 61, 211–219.

Korschinek G., Bergmaier A., Faestermann T., Gerstmann U., Knie K., Rugel G., Wallner A., Dillmann I., Dollinger G. and Von Gostomski C. L. (2010) A new value for the half-life of ^{10}Be by Heavy-Ion Elastic Recoil Detection and liquid scintillation counting. Nucl. Instrum. Methods Phys. Res., Sect. B 268, 187–191.

Koschinsky A. and Halbach P. (1995) Sequential leaching of marine ferromanganese precipitates: genetic implications. Geochim. Cosmochim. Acta 59, 5113–5132.

Koschinsky A. and Hein J. R. (2003) Uptake of elements from seawater by ferromanganese crusts: solid-phase associations and seawater speciation. Mar. Geol. 198, 331–351.

Koschinsky A., Stascheit A., Bau M. and Halbach P. (1997) Effects of phosphatization on the geochemical and mineralogical composition of marine ferromanganese crusts. Geochim. Cosmochim. Acta 61, 4079–4094.

Larson R. L., Pockalny R. A., Viso R. F., Erba E., Abrams L. J., Luyendyk B. P., Stock J. M. and Clayton R. W. (2002) MidCretaceous tectonic evolution of the Tongareva triple junction in the southwestern Pacific Basin. Geology 30, 67–70.

Latta D. E., Gorski C. A. and Scherer M. M. (2012) Influence of Fe^{2+}-catalyzed iron oxide recrystallization on metal cycling. Biochem. Soc. Trans. 40, 1191–1197.

Levasseur S., Frank M., Hein J. and Halliday A. (2004) The global variation in the iron isotope composition of marine hydrogenetic ferromanganese deposits: implications for seawater chemistry?. Earth Planet. Sci. Lett. 224 91–105.

Lu B., Guo H., Li P., Liu H., Wei Y. and Hou D. (2011) Comparison study on transformation of iron oxyhydroxides: based on theoretical and experimental data. J. Solid State Chem. 184, 2139–2144.

Manceau A., Marcus M. A. and Tamura N. (2002) Quantitative speciation of heavy metals in soils and sediments by synchrotron X-ray techniques. In Applications of Synchrotron Radiation in Low-Temperature Geochemistry and Environmental Science (eds. P. A. Fenter, M. L. Rivers, N. C. Sturchio and S. R. Sutton). Mineralogical Society of America, Washington, DC, pp. 341–428.

Manceau A., Lanson M. and Takahashi Y. (2014) Mineralogy and crystal chemistry of Mn, Fe Co, Ni, and Cu in a deep-sea Pacific polymetallic nodule. Am. Mineral. 99, 2068–2083.

Marcus M. A., MacDowell A. A., Celestre R., Manceau A., Miller T., Padmore H. A. and Sublett R. E. (2004a) Beamline 10.3.2 at ALS: a hard X-ray microprobe for environmental and materials sciences. J. Synchrotron Radiat. 11, 239–247.

Marcus M. A., Manceau A. and Kersten M. (2004b) Mn, Fe, Zn and As speciation in a fast-growing ferromanganese marine nodule. Geochim. Cosmochim. Acta 68, 3125–3136.

Marcus M. A., Westphal A. J. and Fakra S. C. (2008) Classification of Fe-bearing species from K-edge XANES data using two-parameter correlation plots. J. Synchrotron Radiat. 15, 463–468.

Martin J. H. and Fitzwater S. (1988) Iron deficiency limits phytoplankton growth in the north-east Pacific subarctic. Nature 331, 947–975.

Martin-Barajas A., Lallier-Verges E. and Leclaire L. (1991) Characteristics of manganese nodules from the Central Indian Basin: relationship with the sedimentary environment. Mar. Geol. 101, 249–265.

McKenzie R. (1971) The synthesis of birnessite, cryptomelane, and some other oxides and hydroxides of manganese. Mineral. Mag. 38, 493–502.

Morford J. L. and Emerson S. (1999) The geochemistry of redox sensitive trace metals in sediments. Geochim. Cosmochim. Acta 63, 1735–1750.

Murad E. and Schwertmann U. (1988) Iron oxide mineralogy of some deep-sea ferromanganese crusts. Am. Mineral. 73, 1395–1400.

Navrotsky A., Mazeina L. and Majzlan J. (2008) Size-driven structural and thermodynamic complexity in iron oxides. Science 319, 1635–1638.

Newville M. (2001) IFEFFIT: interactive XAFS analysis and FEFF fitting. J. Synchrotron Radiat. 8, 322–324.

Nicholson K. and Eley M. (1997) Geochemistry of manganese oxides: metal adsorption in freshwater and marine environments. In Manganese Mineralization: Geochemistry and Mineralogy of Terrestrial and Marine Deposits. Geological Society Special Publication No. 119 (eds. K. Nicholson, J. R. Hein, B. Bu¨hn and S. Dasgupta). The Geological Society, London, pp. 309–326.

Peacock C. L. (2009) Physiochemical controls on the crystalchemistry of Ni in birnessite: genetic implications for ferromanganese precipitates. Geochim. Cosmochim. Acta 73, 3568–3578.

Radic A., Lacan F. and Murray J. W. (2011) Iron isotopes in the seawater of the equatorial Pacific Ocean: new constraints for the oceanic iron cycle. Earth Planet. Sci. Lett. 306, 1–10.

Raiswell R. and Canfield D. E. (2012) The iron biogeochemical cycle past and present. Geochem. Perspect. 1, 1–2.

Ravel B. and Newville M. (2005) ATHENA, ARTEMIS, HEPHAESTUS: data analysis for X-ray absorption spectroscopy using IFEFFIT. J. Synchrotron Radiat. 12, 537–541.

Rouxel O. J., Bekker A. and Edwards K. J. (2005) Iron isotope constraints on the Archean and Paleoproterozoic ocean redox state. Science 307, 1088–1091.

Rouxel O., Shanks, III, W. C., Bach W. and Edwards K. J. (2008) Integrated Fe-and S-isotope study of seafloor hydrothermal vents at East Pacific Rise 9–10 N. Chem. Geol. 252, 214–227.

Sawlan J. J. and Murray J. W. (1983) Trace-metal remobilization in the interstitial waters of red clay and hemipelagic marinesediments. Earth Planet. Sci. Lett. 64, 213–230.

Scholz F., Severmann S., McManus J., Noffke A., Lomnitz U. and Hensen C. (2014) On the isotope composition of reactive iron in marine sediments: redox shuttle versus early diagenesis. Chem. Geol. 389, 48–59.

Schwertman U. and Cornell R. (1991) Iron Oxides in the Laboratory Preparation and Characterization. VCH Publishers.

Schwertmann U. and Cornell R. M. (2000) The Iron Oxides, Iron Oxides in the Laboratory. Preparation and Characterization, second, completely revised and extended ed. Wiley-VCH, pp. 4–18. Segl M., Mangini A., Beer J., Bonani G., Suter M. and Wo¨lfli W. (1989) Growth rate variations of manganese nodules and crusts induced by paleoceanographic events. Paleoceanography 4, 511–530.

Severmann S., McManus J., Berelson W. M. and Hammond D. E. (2010) The continental shelf benthic iron flux and its isotope composition. Geochim. Cosmochim. Acta 74, 3984–4004.

Skulan J. L., Beard B. L. and Johnson C. M. (2002) Kinetic and equilibrium Fe isotope fractionation between aqueous Fe (III) and hematite. Geochim. Cosmochim. Acta 66, 2995–3015.

Somayajulu B. (2000) Growth rates of oceanic manganese nodules: implications to their genesis, palaeo-earth environment and resource potential. Curr. Sci. 78, 300–308.

Takahashi Y., Shimizu H., Kagi H., Yoshida H., Usui A. and Nomura M. (2000) A new method for the determination of Ce^{III}/Ce^{IV} ratios in geological materials; application for weathering, sedimentary and diagenetic processes. Earth Planet. Sci. Lett. 182, 201–207.

Takahashi Y., Manceau A., Geoffroy N., Marcus M. A. and Usui A. (2007) Chemical and structural control of the partitioning of Co, Ce, and Pb in marine ferromanganese oxides. Geochim. Cosmochim. Acta 71, 984–1008.

Tanaka T., Nishimura Y., Kawasaki S.-I., Funabiki T. and Yoshida S. (1987) X-Ray absorption spectroscopy (EXAFS/ XANES) evidence for the preferential formation of isolated VO_4 species on highly photoactive V_2O_5/SiO_2 catalysts. J. Chem. Soc., Chem. Commun., 506–508.

Toner B. M., Santelli C. M., Marcus M. A., Wirth R., Chan C. S., McCollom T. M., Bach W. and Edwards K. J. (2009) Biogenic iron oxyhydroxide formation at Mid-Ocean Ridge hydrothermal vents: Juan de Fuca Ridge. Geochim. Cosmochim. Acta 73, 388–403.

Toner B. M., Berquo T. S., Michel F. M., Sorensen J. V., Templeton A. S. and Edwards K. J. (2012) Mineralogy of iron microbial mats from Loihi Seamount. Front. Microbiol. Chem. 3, 1–18.

Verlaan P. A., Cronan D. S. and Morgan C. L. (2004) A comparative analysis of compositional variations in and between marine ferromanganese nodules and crusts in the South Pacific and their environmental controls. Prog. Oceanogr. 63, 125–158.

Villalobos M., Toner B., Bargar J. and Sposito G. (2003) Characterization of the manganese oxide produced by Pseudomonas putida strain MnB1. Geochim. Cosmochim. Acta 67, 2649–2662.

Wang X., Schloßmacher U., Wiens M., Schro¨der H. C. and Mu¨ller W. E. (2009) Biogenic origin of polymetallic nodules from the Clarion-Clipperton zone in the Eastern Pacific Ocean: electron microscopic and EDX evidence. Mar. Biotechnol. 11, 99–108.

Willenbring J. K. and von Blanckenburg F. (2010a) Long-term stability of global erosion rates and weathering during lateCenozoic cooling. Nature 465, 211–214.

Willenbring J. K. and von Blanckenburg F. (2010b) Meteoric cosmogenic Beryllium-10 adsorbed to river sediment and soil: applications for Earth-surface dynamics. Earth Sci. Rev. 98, 105–122.

Wong J., Lytle F., Messmer R. and Maylotte D. (1984) K-edge absorption spectra of selected vanadium compounds. Phys. Rev. B 30, 5596.

Wu L., Beard B. L., Roden E. E. and Johnson C. M. (2011) Stable iron isotope fractionation between aqueous Fe (II) and hydrous ferric oxide. Environ. Sci. Technol. 45, 1847–1852.

Yoshikawa K. (1991) The relationship between manganese minerals and metallic elements in deep-sea manganese nodules. Mar. Geol. 101, 267–286.

Zhu X. K., O'Nions R. K., Guo Y. L. and Reynolds B. C. (2000) Secular variation of iron isotopes in North Atlantic Deep Water. Science 287, 2000–2002.

Associate editor: Silke Severmann